# Engineering the Mechanical Stability of a Therapeutic Complex between Affibody and Programmed Death-Ligand 1 by Anchor Point Selection

Byeongseon Yang[1,2, §], Diego E. B. Gomes[3, §], Zhaowei Liu[1,2,4], Mariana Sá Santos[1,2], Jiajun Li[1,2],
Rafael C. Bernardi[3,*], and Michael A. Nash*[1,2]

[1] Institute for Physical Chemistry, Department of Chemistry, University of Basel, 4058 Basel, Switzerland
[2] Department of Biosystems Science and Engineering, ETH Zurich, 4056 Basel, Switzerland
[3] Department of Physics, Auburn University, Auburn, Alabama 36849, United States
[4] Present address: Department of Bionanoscience, Delft University of Technology, 2629HZ Delft, the Netherlands

[§] These authors contributed equally to the study
* Correspondence to: michael.nash@unibas.ch; rcbernardi@auburn.edu

## Abstract

Protein-protein complexes can vary in mechanical stability depending on the direction from which force is applied. Here we investigated the mechanical stability of a complex between a binding scaffold called Affibody and immune checkpoint protein Programmed Death-Ligand 1 (PD-L1). We used AFM single-molecule force spectroscopy (AFM-SMFS) with bioorthogonal clickable peptide handles, shear stress bead adhesion assays, molecular modeling, and steered molecular dynamics (SMD) to understand the pulling point dependency of mechanostability of the Affibody:(PD-L1) complex. We observed a wide range of rupture forces depending on the anchor point. Pulling from residue #22 on Affibody generated an intermediate state attributed to partially unfolded PD-L1, while pulling from Affibody's N-terminus generated a force-activated catch bond. Pulling from residue #22 or #47 on Affibody generated high rupture forces, with the complex breaking at up to ~ 190 pN under loading rates of ~$10^4$-$10^5$ pN/sec, representing a ~4-fold increase as compared with low force N-terminal pulling. SMD simulations showed relative tendencies in rupture forces that were consistent with experiments, and through visualization of force propagation networks provided mechanistic insights. These results demonstrate how the mechanical properties of protein-protein interfaces can be controlled by informed choice of site-specific bioconjugation points within molecules, with implications for optimal bioconjugation strategies in drug delivery vehicles.

## Keywords

Biophysics, immobilization, atomic force microscopy, protein engineering, molecular dynamics, molecular recognition

**TOC Graphic**

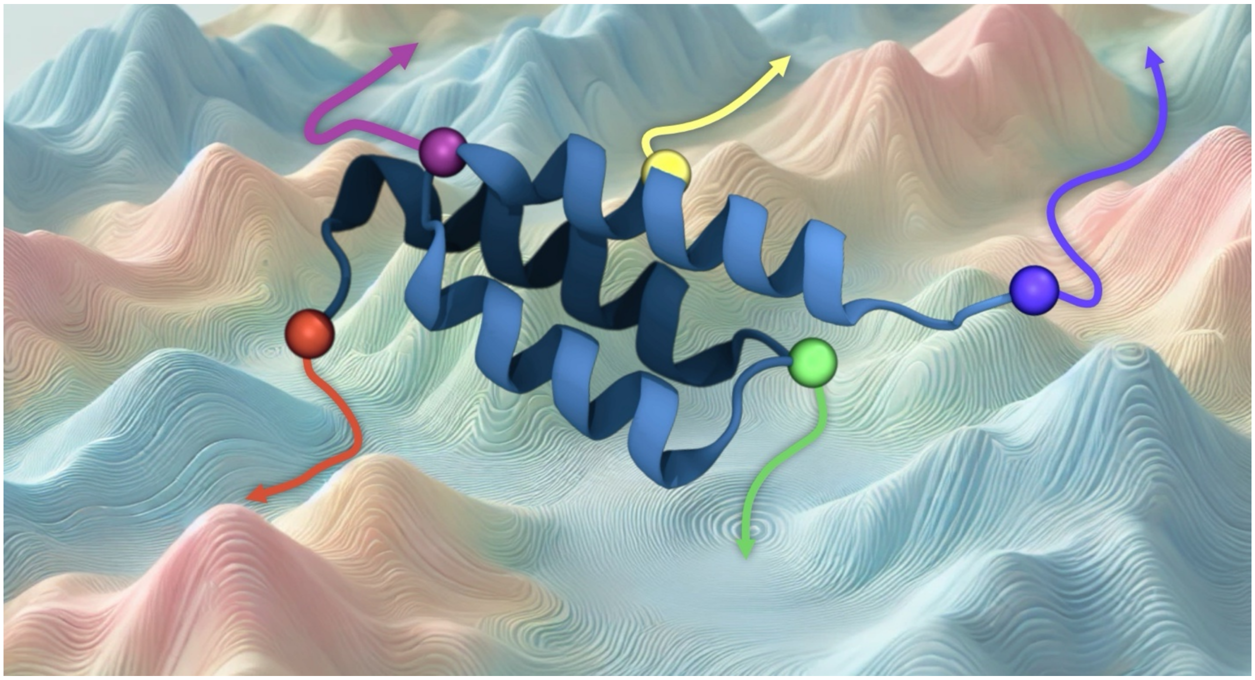

TOC Caption: The mechanical stability of a molecular complex between a binding scaffold (Affibody) and an immune checkpoint protein (PD-L1) was studied while varying the amino position through which force was applied. By choosing the most mechanostable anchor point, bead adhesion under shear stress could be enhanced.

# Introduction

Protein-protein complexes are inherently anisotropic objects, with variably oriented non-covalent interactions that stabilize the structure along different axes. When tension is applied to such a system, the amount of force that the complex can resist before dissociating will significantly depend on the anchor points (i.e. amino acid residues) through which tension is applied. This concept, known as mechanical anisotropy, has been demonstrated on folded protein domains[1–5], nucleic acids[6] and protein-protein complexes[7–11], among others[12]. Although this conceptual framework has existed in the molecular biophysics community for years, its potential for enhancing binding strength for applications in drug delivery is less explored. In particular, for nanoparticle and cell-based therapies, binding proteins attached to the particle or cell surface to achieve specific targeting are subjected to hydrodynamic shear forces inside the body. If these binding proteins have been optimized for high affinity interactions at equilibrium (i.e. in the absence of force), they can perform poorly and unbind at low forces when exposed to shear stress.[13,14] Therefore, in developing drug delivery systems for operation under conditions of hydrodynamic flow, the concept of imparting mechanical stability through anchor point selection to improve interaction and adhesion strength is of significant interest.

Non-immunoglobulin (non-Ig) scaffolds have significant potential as next-generation therapeutics due to their small size and ease of production.[15,16] The Affibody (AFF) scaffold based on the Z-domain of *S. aureus* protein A in particular is a promising alternative scaffold comprising three bundled α-helices.[17–19] Solvent accessible residues contained within α-helices 1 and 2 of the AFF scaffold have been mutagenized to isolate AFF variants with specific binding activity towards several therapeutic drug targets, for example, programmed cell death ligand 1 (PD-L1),[20–22] an immune checkpoint protein and major target in cancer immunotherapy.[23–26] In fact, an AFF variant that binds PD-L1 with high affinity was reported as a potential candidate for *in vivo* tumor imaging with good specificity and rapid clearance.[20,21]

AFM-based single-molecule force spectroscopy (AFM-SMFS) is a powerful technique to study the mechanical responses of protein interactions under force.[27,28] Single protein-protein complexes can be dissociated under mechanical tension to study a variety of mechanical responses, such as classical slip bonds, force-activated catch bonds, intermediate unfolding states, and other structural transitions.[29–33] Recently we reported on a protein bioconjugation and surface chemical approach relying on non-canonical amino acid (NCAA) incorporation and click chemistry to install peptide handles onto single side chains, and apply tension at any position within a protein sequence.[7] The peptide handle[10,11,34] called Fgβ served as an orthogonal pulling point within the sequence that could be recognized by an SdrG domain attached to a cantilever tip, allowing us to study the anchor point dependence of mechanostability in protein-protein complexes.

Here, using AFM-SMFS we analyzed the mechanical stability of the AFF:(PD-L1) complex when pulled from five different anchor points on AFF (i.e. five different pulling points, respectively). Combined with in silico SMFS, which is based on steered molecular dynamics (SMD) simulations, we observed different mechanical responses and changes in the unbinding pathway depending on the pulling point. We further compared the most and least stable pulling points using a bead-based shear stress adhesion assay[35] to analyze how these single-molecule mechanical properties manifest under conditions of multivalent collective binding under the influence of shear forces.[35–37] We found that in particular, pulling AFF from central positions within the sequence generated higher resistance to mechanical load (i.e. higher rupture forces), which resulted in enhanced bead adhesion under shear flow. The SMD simulations provide crucial information about the mechanical properties of the (PD-L1):AFF complex, confirming the mechanical anisotropy and revealing differences in unfolding behavior, rupture forces, force propagation pathways and contact interactions depending on the pulling points.

# Results/Discussion

### Selection of Pulling Points, Protein Preparation, and AFM Measurement Setup.

An AFF variant that binds PD-L1 was previously engineered by random mutagenesis and screening of solvent-accessible residue variants within the first two α-helices of AFF.[20,21] In our study, recombinant AFF and the extracellular domain of human PD-L1 (PD-L1-ECD) were prepared by overexpression in *E. coli* to first confirm binding (**Figure S1** and **Figure S2**).[38] Since AFF is only 59 amino acids long and consists of three α-helices, there were limited positions within the sequence where we could install orthogonal pulling points while minimizing perturbations to the binding epitope. Analyzing structural models of AFF, we determined that potential positions for pulling point insertion would be at: 1) the N-terminus; 2) within the loop between α1 and α2 helices; 3) within the loop between α2 and α3 helices; 4) solvent accessible residues on α3 helix; and 5) at the C-terminus (**Figure 1A**, **1B, and Figure S3**). Based on these considerations, five pulling points within AFF were chosen by selecting one residue from each of these regions. The chosen pulling points on AFF were the N-terminus (M1), C-terminus (G60) and three internal sequence positions (N22, S40, S47; **Figure 1B**). In all experiments, the PD-L1 extracellular domain was always anchored through its C-terminus to mimic its orientation on the cell surface.

To dissociate the (PD-L1):AFF complex by applying tension through a given pulling point, we used NCAA incorporation into AFF combined with click chemistry to install a peptide pulling handle at a given position.[28] We first introduced an Amber stop codon into the gene cassette encoding AFF at the desired position. We then employed site-specific incorporation of p-Azido-L-phenylalanine (pAzF) by amber suppression in *E. coli*, and confirmed incorporation by high resolution mass spectrometry (HR-MS) (**Figure S4**). To attach the Fgβ peptide as a pulling handle, a synthetic Fgβ peptide containing a C-terminal dibenzocyclooctyne (DBCO) group was conjugated onto the desired position of AFF using a copper-free click reaction between the azide group of pAzF and the DBCO group on Fgβ (**Figure 1C**). Following conjugation, we characterized Fgβ-AFF conjugates using SDS-PAGE and HR-MS analyses (**Figure S4**). For the N-terminal pulling points, AFF was separately prepared as a fusion with an N-terminal Fgβ peptide sequence (**Figure S5**). Each AFF pulling point variant was separately cloned with a single amber codon at the given position, produced in *E. coli*, conjugated with Fgβ and measured in separate AFM-SMFS experiments.

For the AFM experimental setup, we produced the PD-L1 extracellular domain with a C-terminal SpyTag (PD-L1-SpyTag) (**Figure S6**). As PD-L1 is naturally a transmembrane protein with C-terminal transmembrane domain, SpyTag was fused to the C-terminal side of the recombinant extracellular PD-L1 domain to mimic the natural anchor point of PD-L1 in the membrane. The SpyTag was then further conjugated to a SpyCatcher domains *via* spontaneous isopeptide bond formation.[39,40] SpyCatcher was produced as polyprotein (SpyCatcher-FLN-ELP-ybbR) where the fourth domain of Dictyostelium discoideum F-actin cross-linking filamin (FLN) served as an SMFS fingerprint, an elastin-like polypeptide (ELP) sequence served as a flexible linker, and a ybbR tag facilitated site-specific covalent surface immobilization (**Figure S6**).[39–41] PD-L1-SpyTag was conjugated to SpyCatcher-FLN-ELP-ybbR and further site-specifically and covalently immobilized onto coenzyme A (CoA)-functionalized coverglass substrates *via* ligation by 4′-phosphopantetheinyl transferase (SFP) (**Figure 1D** and **Figure S6**). For the free diffusion measurement setup, SD-repeat protein G (SdrG) from *S. epidermidis* was prepared as a fusion protein of the form SdrG-FLN-ELP-ybbR, and immobilized onto silicon nitride cantilever tips *via the* ybbR tag. Cantilevers functionalized in this manner could be used to bind Fgβ-AFFs (**Figure 1D**) and dissociate them from surface-immobilized PD-L1 by applying tension through the various pulling points.[7] SdrG binds Fgβ with moderate equilibrium binding affinity ($K_D$ ~400 nM) which enabled rapid exchange of Fgβ-conjugated molecules on the cantilever tip. This measurement approach is able to constantly probe fresh molecules on both the surface (by actuating the AFM X-Y stage) and cantilever (by reversible ligand dissociation/exchange), thereby avoiding irreversible protein unfolding.[7,28,34,42] Since the SdrG:Fgβ complex can withstand up to ~2 nN of force prior to rupture, it is capable of breaking the (PD-L1):AFF binding interface. With this AFM setup, (PD-L1):AFF complexes with five different pulling geometry were probed at four different pulling speeds ($0.1 \times 10^3$, $0.4 \times 10^3$, $1.6 \times 10^3$, $6.4 \times 10^3$ nm $s^{-1}$) using constant speed AFM-SMFS. All data traces were filtered for two 34 nm contour length increments which originated from the two FLN fingerprint domains, one from the SdrG bound to the cantilever, and one from the PD-L1 bound to the surface. This fingerprint filtering method allowed us to identify single-molecule level interactions (**Figure 1E**) in large datasets consisting of tens of thousands of AFM force-extension curves. FLN unfolding was followed by rupture of (PD-L1):AFF complex. In some cases, we found that the (PD-L1):AFF complex rupture force range was lower than the unfolding force of FLN. Therefore, data traces with no FLN unfolding were also analyzed in the case of the N-terminal pulling point (M1, red) (**Figure 1E**).

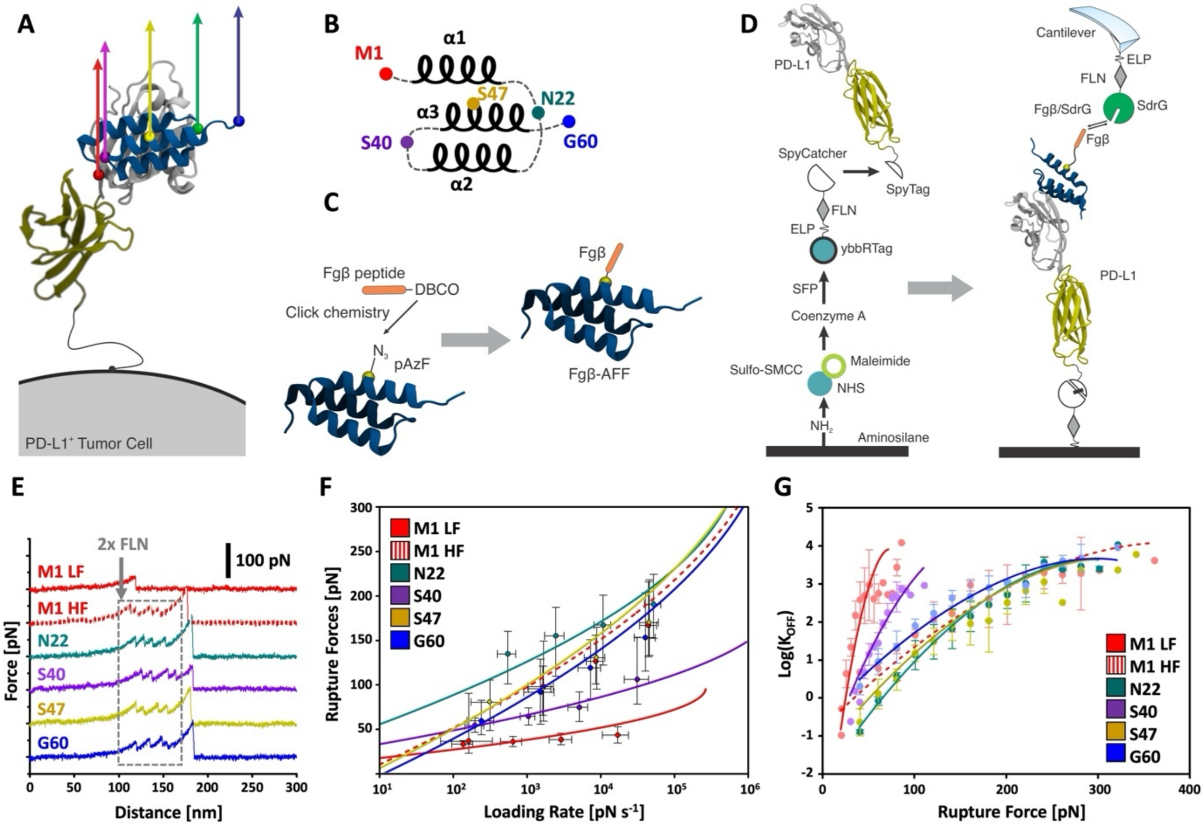

**Figure 1.** Pulling point selection and mechanostability of the (PD-L1):AFF complex analyzed by single-molecule AFM. (A) Prediction of AFF structure in complex with PD-L1 by AlphaFold. Pulling points on AFF are indicated as colored spheres. The extracellular domain of PD-L1 is fixed at the C-terminus according to the natural anchor geometry on the cell surface. (B) AFF consists of three α helices connected by short flexible loops. The pulling points were selected from the termini, loops connecting α helices, and in the middle of the α3 helix. (C) Bioorthogonal conjugation of a fibrinogen β (Fgβ) peptide to AFF via non-canonical amino acid incorporation and click chemistry. P-azido-phenylalanine was introduced at a single desired pulling point using amber suppression and clicked to a synthetic Fgβ-DBCO peptide. (D) Schematic illustration of the surface chemistry, site-specific protein immobilization, and AFM setup with freely diffusing receptor system. (E) Typical AFM force−extension traces of the (PD-L1):AFF complex rupture traces under five different pulling geometries, including M1 high force population (M1 HF; Dashed line) and M1 low force

population (M1 LF; Solid line). Each of curves were plotted with 100 pN offsets. Unfolding of two FLN fingerprint domains (Gray dotted box and gray arrow) was used to filter the curves for specific single-molecule interactions. For the N-terminal (low force) pulling points, the (PD-L1):AFF interaction was not sufficiently strong to unfold the FLN fingerprint domains. (F) Dynamic force spectra of (PD-L1):AFF complex rupture events. Black-lined circles represent the median rupture force/loading rate at each pulling speed of $0.1 \times 10^3$, $0.4 \times 10^3$, $1.6 \times 10^3$, and $6.4 \times 10^3$ nm $s^{-1}$. Error bars are ±1 s.d. Solid and dashed lines are least square fits to the Dudko-Hummer-Szabo (DHS) model. (G) The force-dependent off rate of the (PD-L1):AFF complex was plotted against rupture force and fitted to DHS model extract Δx, $k_0$ and ΔG.

**Table 1.** Energy landscape parameters of the (PD-L1):AFF complex rupture under different pulling geometries by AFM-SMFS with Bell-Evans (BE) and Dudko-Hummer-Szabo (DHS) model fitting and the dissociation constant values measured by beads-based equilibrium binding affinity analysis via flow cytometry. [a]HF: High force population, [b]PU: Partial unfolding.

| **Pulling Points** | **Δx [nm] (BE)** | **Δx [nm] (DHS)** | **Ln($k_{off}$) (BE)** | **Ln($k_{off}$) (DHS)** | **ΔG [$k_BT$] (DHS)** | **Rupture force [pN] $0.1\times10^3$ nm $s^{-1}$** | **Rupture force [pN] $6.4\times10^3$ nm $s^{-1}$** | **$K_D$ [nM]** |
|---|---|---|---|---|---|---|---|---|
| **M1** | 2.0 ± 0.2 | 1.3 ± 0.2 | − 11.8 ± 1.8 | − 4.5 ± 1.8 | 15.3 ± 2.0 | 34 ± 4 | 44 ± 9 | 28.1 ± 13.8 |
| HF[a] | 0.18 ± 0.00 | 0.25 ± 0.03 | − 0.2 ± 0.2 | − 1.7 ± 0.8 | 13.0 ± 0.9 | 37 ± 34 | 167 ± 43 | |
| **N22** | 0.35 ± 0.03 | 0.36 ± 0.03 | − 7.6 ± 1.0 | − 5.2 ± 0.7 | 15.8 ± 0.8 | 135 ± 30 | 191 ± 36 | 22.3 ± 4.5 |
| PU[b] | 0.87 ± 0.05 | 1.0 ± 0.1 | − 16.6 ± 1.3 | − 13.3 ± 1.5 | 25.1 ± 1.5 | 100 ± 14 | 121 ± 16 | |
| **S40** | 0.65 ± 0.02 | 0.78 ± 0.25 | − 5.2 ± 0.3 | − 5.7 ± 1.8 | 18.2 ± 4.0 | 55 ± 8 | 106 ± 37 | 22.5 ± 7.8 |
| **S47** | 0.23 ± 0.03 | 0.23 ± 0.02 | − 1.2 ± 0.8 | − 1.5 ± 0.6 | 12.6 ± 0.5 | 81 ± 28 | 170 ± 42 | 35.5 ± 7.5 |
| **G60** | 0.22 ± 0.01 | 0.24 ± 0.02 | − 0.6 ± 0.1 | − 1.0 ± 0.5 | 12.3 ± 0.4 | 60 ± 19 | 154 ± 44 | 37.1 ± 11.3 |

### Alteration of Pulling Geometry Drastically Changes the Unbinding Energy Landscape.

We analyzed the (PD-L1):AFF complex rupture events under different pulling geometries. In total we conducted ten different AFM measurement trials using two replicates of five pulling points, collecting 109,067 total AFM-SMFS force-extension traces in total. Of these, 33,365 curves were selected for further analysis, and finally the contour length and the quality filters were applied generating 4,868 rupture force data points. Final data points were plotted as a function of the loading rate (**Figure 1F, S7, and S8**), demonstrating how the mechanostability of the (PD-L1):AFF complex strongly depends on the pulling point. Depending on the anchor point residue on AFF, different characteristics were observed in terms of rupture force ranges, loading rate dependencies, the presence of multiple unbinding pathways, and energy profile parameters (**Figure 1F** and **1G**), as discussed in detail below.

For pulling point M1, the rupture force range was the lowest at all pulling speeds compared to the other pulling geometries, ranging from 34 ± 4 pN at $0.1 \times 10^3$ nm $s^{-1}$ to 44 ± 9 pN at $6.4 \times 10^3$ nm $s^{-1}$ (**Table 1**). Interestingly, we observed a new rupture force population as pulling speed increased. This new population showed much higher rupture forces, more similar to the other pulling points such as S47 and G60 and with similar loading rate dependency. The ratio of this new high force population (M1 HF) to low force population (M1 LF) increased as the pulling speed increased, showing catch bond-like behavior (**Figure S8**) as manifested in a constant speed pulling protocol.[31,43]

Meanwhile, the pulling point N22 generated the most mechanostable (PD-L1):AFF interaction, with the highest rupture forces across all pulling speeds from 135 ± 30 pN at 0.1 x $10^3$ nm $s^{-1}$ to 191 ± 36 pN at 6.4 x $10^3$ nm $s^{-1}$ (**Table 1**). This force range was ~4.0-4.3 fold higher than the low force population found for pulling point M1. Pulling point N22 was furthermore characterized by an alternative unbinding pathway with an intermediate unfolding state that was not found in any other pulling geometry. We regularly detected an additional intermediate unfolding peak prior to final rupture for pulling point N22 (**Figure S9**). The contour length increment associated with this unfolding event was found to be ~14 nm. Assuming ~0.35 nm / amino acid in contour length space, this corresponds to an unfolding event of ~40 amino acids. If we assigned this unfolding event to a structural transition within AFF, it would correspond to unfolding of ~68% of the AFF length while maintaining strong binding to PD-L1 (**Figure S9**). We judged this scenario unlikely, and therefore assigned the intermediate unfolding increment observed for the N22 pulling point to partial unfolding of PD-L1. Therefore, we concluded that mechanostability of the (PD-L1):AFF complex when pulled from point N22 was significantly high such that force applied to AFF can partially unfold PD-L1 prior to unbinding from PD-L1. It is important to note here that our recombinant PD-L1 consists of two separate domains that could conceivably (un)fold independently from one another.

For pulling points S40, S47, and G60, the (PD-L1):AFF complexes showed typical unimodal behavior without intermediate unfolding events or catch bond behavior. While S40 exhibited low to moderate rupture forces, ranging from 55 ± 8 pN at 0.1 x $10^3$ nm $s^{-1}$ to 106 ± 37 pN at 6.4 x $10^3$ nm $s^{-1}$ (**Table 1**), both S47 and G60 showed low to high force rupture rupture events with a steep loading rate dependency. At a slow pulling speed of 0.1 x $10^3$ nm $s^{-1}$, weak interactions were observed with a rupture force of 81 ± 28 pN and 60 ± 19 pN for S47 and G60, respectively, however at the high pulling speed of 6.4 x $10^3$ nm $s^{-1}$, strong interactions were observed, as much as 170 ± 42 pN and 154 ± 44 pN for S47 and G60, respectively.

Unbinding energy landscape parameters generated by the various pulling geometries were estimated by parameter fitting using Bell-Evans (BE)[44,45] and Dudko-Hummer-Szabo (DHS)[46] models. The relevant parameters were the distance to the energy barrier (Δx) and the off-rate ($k_{off}$) for the BE model (**Figure S7 and S8**). For the DHS model, we obtained the energy barrier heights (ΔG), Δx and $k_{off}$ in order to generate a force-dependent off-rate plot (**Figure 1G**). The estimated parameters from both models are listed in **Table 1**. We note that these models are highly simplified and assume a simple two-state system, which is not the case for our complex as the intermediate events for pulling point N22 and catch bond behavior for pulling point M1 demonstrate. Furthermore, differences in the fitted zero-force $k_{off}$ are spurious since for our system all anchor point variants have the same equilibrium binding affinity (see below) and presumably very similar equilibrium off-rates. Nonetheless, the model fitting demonstrated that unbinding of the (PD-L1):AFF complex from different pulling points exhibits different energy profiles, with fitted Δx parameters varying up to ~9-fold and ΔG varying up to ~1.5-fold depending on the pulling point. It is worth noting that the mechanical stability of the complex is determined by both height and the shape of the unbinding energy landscape. Combination of the high barrier height and short distance to the transition state contributed to high resistance to external force for the most mechanostable pulling geometry N22. Pulling geometries S40 has the highest energy barrier, but the long Δx generated overall lower mechanostability than N22. Pulling geometry M1 LF meanwhile exhibited the longest Δx with the lowest mechanostability. Although pulling from S47 and G60 generated the lowest energy barriers, a very short Δx contributed to steep loading rate dependency for these points, giving rise to the high mechanostability at high pulling speeds.

### Minimal Dependency of Conjugation Points on Equilibrium Binding Affinity.

To investigate the effect of anchor point engineering on equilibrium binding behavior, we performed beads-based flow cytometric binding assays to measure the equilibrium dissociation constant ($K_D$) between (PD-L1):AFF using a fluorescent dye conjugated to the bioorthogonal side chain used for pulling in the AFM experiments. AFF variants were prepared where FAM-DBCO was conjugated to each of five pulling points (instead of Fgβ) using the same click reaction. PD-L1 was immobilized on amine-functionalized polystyrene (PS) beads in the same way for AFM setup (**Figure 2A**). The AFF-FAM conjugates were titrated across a concentration range and the fraction of fluorescently labeled beads was analyzed by flow cytometry to extract fitted $K_D$ values (**Figure 2B**) for each AFF variant. We found $K_D$ values to be 28.1 ± 13.8 nM, 22.3 ± 4.5 nM, 22.5 ± 7.8 nM, 35.5 ± 7.5 nM, and 37.1 ± 11.3 nM for AFF variants M1, N22, S40, S47, and G60, respectively (**Figure 2B**). Despite the quantitative and qualitative differences in unbinding behavior observed for the various pulling points in the AFM experiments, the equilibrium analysis revealed that binding affinity was not significantly changed by introduction of the bioorthogonal azide group at the respective position. This also validated the rationale for pulling point selection, where we targeted only flexible loops, flexible termini or solvent exposed side chains in AFF located away from the binding interface with PD-L1.

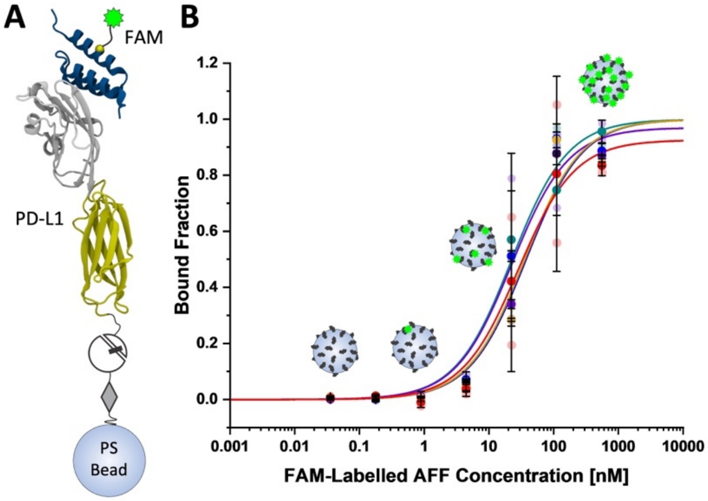

**Figure 2.** Bead-based equilibrium binding affinity analysis via flow cytometry. (A) Schematic illustration of surface chemistry, site-specific protein immobilization, and fluorescent dye conjugation. (B) Binding curves and the fitting to determine binding affinity of the (PD-L1):AFFibody complex with different conjugation points. Error bars are ±1 s.d.

### Mechanical Insight of (PD-L1):AFF Complex Rupture by SMD.

Next we used Steered Molecular Dynamics (SMD) to simulate the (PD-L1):AFF system while applying tension through the same pulling points as in the AFM-SMFS experiments (**Figure 1A**). Each geometry was probed at three constant pulling speeds by SMD (2.5 x $10^7$ , 2.5 x $10^8$, and 2.5 x $10^9$ nm $s^{-1}$). We examined and compared the unfolding and rupture events, and plotted against the loading rate together with the experimental dataset on a single set of axes (**Figure 3A**).[47] Consistent with the AFM-SMFS measurements, our SMD simulations demonstrated significant mechanical anisotropy, with different pulling geometries exhibiting distinct characteristics in terms of protein unfolding, rupture force ranges, loading rate dependencies, unbinding pathways, and force profiles.

Analysis of the (PD-L1):AFF simulated force traces revealed multiple peaks along the extension. A visual inspection of the SMD trajectories and of the nearest snapshot prior to rupture (**Figure 3B**) revealed sequential unfolding of the α1 helix when pulling from the N-terminus (**Videos S1-5**). N-terminal pulling also resulted generally in the lowest rupture forces across all simulated pulling speeds (**Table 2**), and the broadest spread of loading rates for a given pulling speed (**Figure 3A**). When pulling from the C-terminus, we also regularly observed peeling of the α3 helix. Inspection of the forces and (PD-L1):AFF contact area for each pulling point reveals that for internal pulling residues (N22, S40, and S47), the peak force frequently coincided with complex rupture and loss of contact between the proteins. In the case of the N- and C-terminal pulling points (M1 and G60), single step breakage was less frequently observed, with the proteins exhibiting intermediate unfolding and remaining bound following the peak force (**Figure S10, S11, and S12**).

For pulling points N22, S40 and S47, the (PD-L1):AFF complex showed typical unimodal behavior without additional unfolding events or catch bond-like behavior. Pulling from N22 showed a stable interaction of the complex and generated the second highest rupture forces at all the simulated pulling speeds (e.g., 510 ± 68 nN at 2.5 x $10^9$ nm $s^{-1}$ (**Table 2**)). These simulated rupture values were ~1.5 fold higher than the low force population of the $N_{terminal}$ pulling point. Pulling point N22 was not found in the simulations to generate partial unfolding of PD-L1 as was observed in the experiments (**Figure S9**). Similarly to AFM-SMFS, pulling from S40 showed a low to moderate range of ruptures (344 ± 44 nN at 2.5 x $10^9$ nm $s^{-1}$), while S47 showed the highest rupture force range with strong loading rate dependency (579 ± 44 nN at 2.5 x $10^9$ nm $s^{-1}$).

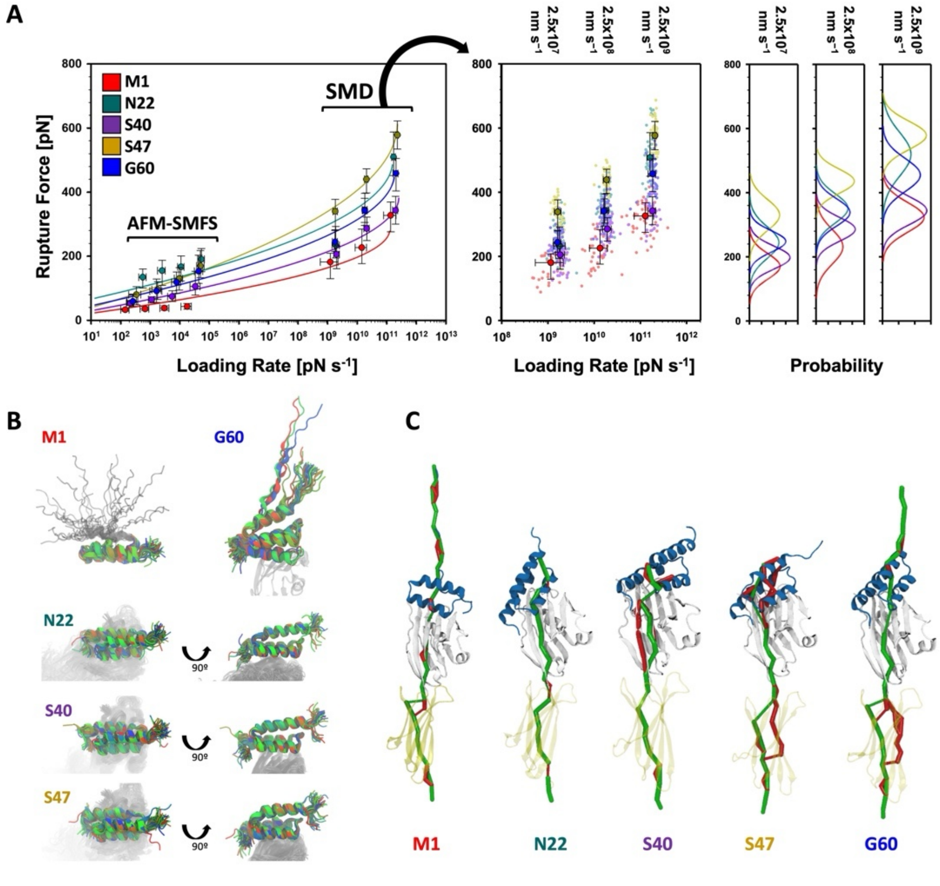

**Figure 3. Steered molecular dynamics simulations of pulling (PD-L1):AFFibody complex from different anchor points.** (A) Combined experimental and simulated dynamic force spectra and the histogram of the (PD-L1):AFFibody complex rupture. Black-lined circles represent the median rupture force/loading rate at each pulling speed. Error bars are ±1 s.d. Solid lines in dynamic force spectra are least square fits to the DHS model. Solid lines in histogram are Gaussian fit. (B) The closest trajectory frame to the peak force measured from all replicas at 2.5x$10^7$ nm $s^{-1}$ after fitting to AFF's backbone atoms from

residues 5 to 55. When pulling from the N-terminal, fitting was limited to residues 25 to 55 due to unfolding of α1. C and N terminals have 40 replicas each, while N22, S40 and S47 have 48 replicas each. (C) Predominant force propagation pathways. For most replicas and pulling points (except C-terminal) the optimal force propagation path (green) from the pulling residue to the anchor exits the AFF through Asp36$_{AFF}$, passing through Arg96$_{PD\text{-}L1}$, and then propagating up to Gly93$_{AFF}$ and crossing to PD-L1 through Lys112$_{PD\text{-}L1}$ or Val113$_{PD\text{-}L1}$. Suboptimal paths (red) less frequently take alternative routes through the interface. While pulling from Ser47$_{AFF}$, most replicas commonly showed two suboptimal pathways that may reinforce the complex and explain its higher resilience. The width of the force propagation pathways is weighted by the correlation strength in the dynamic network.

**Table 2.** Energy landscape parameters of the (PD-L1):AFFibody complex rupture with different pulling geometries from SMD simulation with Bell-Evans (BE) model and Dudko-Hummer-Szabo (DHS) model fitting.

| **Pulling Points** | **Δx [nm] (BE)** | **Δx [nm] (DHS)** | **Ln($k_{off}$) (BE)** | **Ln($k_{off}$) (DHS)** | **ΔG [$k_BT$] (DHS)** | **Rupture force [pN] $2.5 \times 10^9$ nm s$^{-1}$** |
|---|---|---|---|---|---|---|
| **M1** | 0.31 ± 0.04 | 0.79 ± 0.02 | 1.8 ± 1.4 | − 5.7 ± 1.8 | 27.3 ± 6.0 | 328 ± 46 |
| **N22** | 0.28 ± 0.07 | 0.51 ± 0.07 | − 4.8 ± 4.1 | − 8.0 ± 1.1 | 31.2 ± 6.4 | 510 ± 68 |
| **S40** | 0.31 ± 0.03 | 0.60 ± 0.07 | − 0.4 ± 1.3 | − 4.4 ± 1.6 | 28.2 ± 1.4 | 344 ± 44 |
| **S47** | 0.18 ± 0.02 | 0.36 ± 0.02 | − 0.0 ± 1.2 | − 4.1 ± 0.9 | 27.3 ± 0.8 | 579 ± 44 |
| **G60** | 0.25 ± 0.03 | 0.53 ± 0.06 | − 0.8 ± 1.8 | − 6.1 ± 2.0 | 29.5 ± 2.7 | 459 ± 51 |

### Force propagation pathway analysis

We used generalized-correlation-based dynamical network analysis[48] to extract correlations of motion from multiple (PD-L1):AFF simulation replicas for each pulling point and characterize the force propagation pathways[9]. For most replicas and pulling points (except C-terminal), the optimal force propagation pathways (**Figure 3C**, blue) between the AFF pulling point and the anchor point at PD-L1's C-terminus exited AFF through residue Asp36$_{AFF}$, passing through Arg96$_{PD\text{-}L1}$, and propagating up to Gly93$_{AFF}$ before crossing to PD-L1 through Lys112$_{PD\text{-}L1}$ or Val113$_{PD\text{-}L1}$. The suboptimal paths (**Figure 3C**, red) less frequently took alternative pathways across the binding interface. While pulling from Ser47$_{AFF}$, most replicas showed two suboptimal pathways that may reinforce the complex and explain its higher force resilience. The multiplicity of optimal and suboptimal pathways is also observed for the G60 anchor point, but these pathways do not affect the binding dynamics or enhance the complex's mechanical resilience, as they are confined to the IgC domain. In contrast, significant force dissipation at the interface is seen only with S47 anchoring (**Figure S13**), consistent with previous studies on force dissipation in systems such as silk fibers.

Aligned with the AFM-SMFS experiments, these findings explain the different rupture force populations observed as pulling speed increased. This finding suggests that the distribution of forces along different pathways can either concentrate stress at specific residues, leading to a peeling or unfolding mechanism, or spread the forces more evenly across the interface, resulting in a clean rupture. This behavior highlights the interplay between optimal and suboptimal pathways in determining the mechanical stability of the complex under different pulling conditions. However, the simulations did not capture two distinct rupture force populations as was observed in AFM-SMFS for pulling point M1 (**Figure S8**).

To investigate the intermediate unfolding event observed experimentally (**Figure S9**), we tested the unfolding force of the IgC domain under similar pulling conditions. In some cases, the rupture force of S47, and occasionally N22, overlapped with the IgC unfolding force, suggesting that the IgC domain may unfold under high-force conditions. Since N22 shows higher rupture forces compared to other pulling points, at lower pulling rates it is likely that unfolding was experimentally detected only when pulling from N22. **Figure S14** illustrates this behavior, highlighting the overlap in force profiles and their correlation with experimental results.

## Enhanced microbead adhesion under shear stress

We next investigated how these anisotropic stability effects would influence microbead adhesion strength that arises from collective and multivalent interactions. We chose three internal anchor points for microbead adhesion assays based on the AFM-SMFS and SMD simulations: N22 (highest mechanostability by AFM-SMFS); S47 (highest mechanostability by SMD); and S40 (low mechanostability). Although M1 showed the lowest rupture force population in both AFM-SMFS and SMD simulations, it was not selected for the bead assays due to catch bond behavior found in the AFM-SMFS experiments (**Figure S8**).

We used the hydrodynamic shear-based spinning disk assay (SDA)[35,37] where (PD-L1)-modified beads were deposited onto AFF-modified coverglass surfaces and exposed to a rotational hydrodynamic shear field. We designed and prepared a Cys-SpyCatcher protein by introducing one cysteine in the middle of the short linker connecting FLN and SpyCatcher (**Figure S15**). Cys-SpyCatcher was DBCO-functionalized using DBCO-PEG$_4$-maleimide and conjugated to AFF at the desired position via click chemistry (**Figure 4A** and **S15**). AFF-pAzF-DBCO-Cys-SpyCatcher for each of these three internal conjugation points was then immobilized onto amino-functionalized coverglass disks in the same way as was used in the AFM-SMFS setup. PD-L1 was immobilized onto PS beads in the same way as previously mentioned (**Figure 4A**).

(PD-L1)-modified PS beads were adhered onto the AFF-immobilized coverglass (**Figure 4B**). As the disk was spun, beads experienced a gradient of shear stress that increased from the disk center to the edge. The higher shear stress at the outer edge of the disk disrupted the (PD-L1):AFF interactions, resulting in loss of bead adhesion. The sigmoidal decrease in bead density as a function of the distance from the disk center was plotted and analyzed to determine $\tau50$, a parameter that represents the amount of shear stress required to detach 50% of the beads.

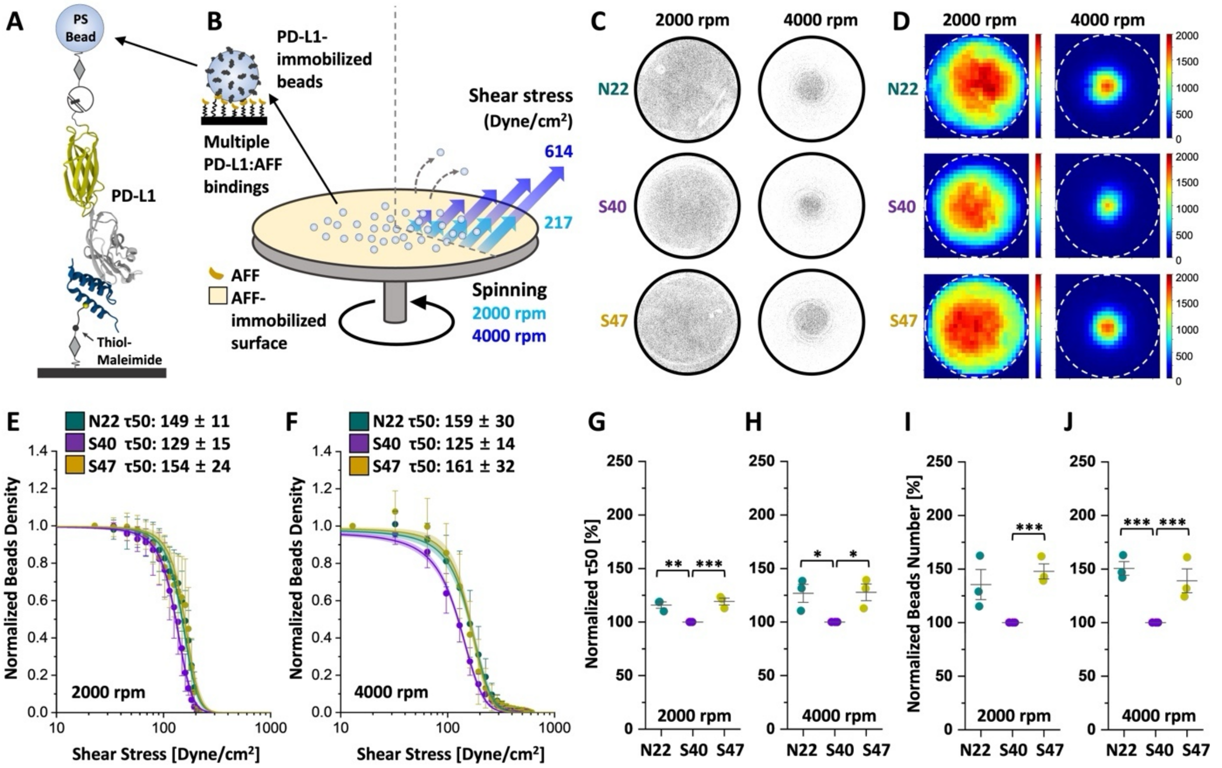

**Figure 4.** Analysis of microbead adhesion under shear flow mediated by AFF:(PD-L1) complexes. (A) Schematic illustration of surface chemistry, site-specific protein conjugation, and immobilization. (B) PS beads coated with PD-L1 are adhered to an AFF-modified glass disk and exposed to a shear stress generated by spinning. Shear stress is linearly proportional to radius with the values of 217 Dyne/cm$^2$ for 2000 rpm (Cyan) and 614 Dyne/cm$^2$ for 4000 rpm (Dark blue) at the edge of the disk. (C) Typical raw images and (D) beads density map of AFF-modified disks with three different AFF anchor points following spinning at 2000 or 4000 rpm. Normalized bead density plots *vs.* shear stress for the three different AFF anchor points at spinning speeds of (E) 2000 and (F) 4000 rpm. Plotted data from six glass disks were fitted with a sigmoid model to extract τ50, the shear stress required to detach half the bead population. Comparison of normalized τ50 of the AFF:(PD-L1) complex with three different conjugation points at the spinning speeds of (G) 2000 and (H) 4000 rpm. Comparison of normalized total beads number of the AFF:(PD-L1) complex with three different conjugation points at the spinning speeds of (I) 2000 and (J) 4000 rpm. Shades indicate 95% confidence intervals from fitting. Teal: AFF-N22pAzF, Purple: AFF-S40pAzF, and Dark yellow: AFF-S47pAzF. n.s. $p \geq 0.05$; *$p < 0.05$; **$p < 0.01$; ***$p < 0.005$.

Three independent replicates of SDA analyses with two glass disks for each replicate were performed for the three internal conjugation points. As a result, images of disks were taken with low (2000 rpm) and high (4000 rpm) spinning speeds (**Figure 4C, D**). Bead detachment was only observed at the very outer edge of the disk after spinning at the low speed (**Figure 4C & D,** left). At the higher speed, we found that the central area over which the beads remained attached was larger for N22 and S47 than for S40 (**Figure 4C & D,** right). We used image analysis to calculate and plot the normalized bead density against the shear stress, and fit the sigmoids to a probabilistic model equation to extract final τ50 values for low (**Figure 4E**) and high (**Figure 4F**) spinning speeds. These data demonstrate that when AFF was immobilized through N22 or S47, the beads adhered to the disk with τ50 value of 149 ± 11 and 154 ± 24 dyne cm$^{-2}$ at 2000 rpm and 159 ± 30 and 161 ± 32 dyne cm$^{-2}$ at 4000 rpm, respectively. When AFF was immobilized through S40, we measured lower τ50 values of 129 ± 15 and 125 ± 14 dyne cm$^{-2}$ at 2000 and 4000 rpm, respectively. Normalized τ50 value for each replicate showed statistical significance at both low (**Figure 4G**) and high speeds (**Figure 4H**). The total number of beads remaining on the disk after spinning also showed a consistent trend and similarly reported on the stability of the AFF:(PD-L1) interaction dependent on the anchor point (**Figure 4I, J**). Therefore, the results from the microbead adhesion assays were consistent with AFM-SMFS and SMD simulations for the loading rate range >10$^4$ pN s$^{-1}$, where the rupture force of the S47 pulling point was similar to or slightly higher than that of N22, and the rupture force of S40 was lower.

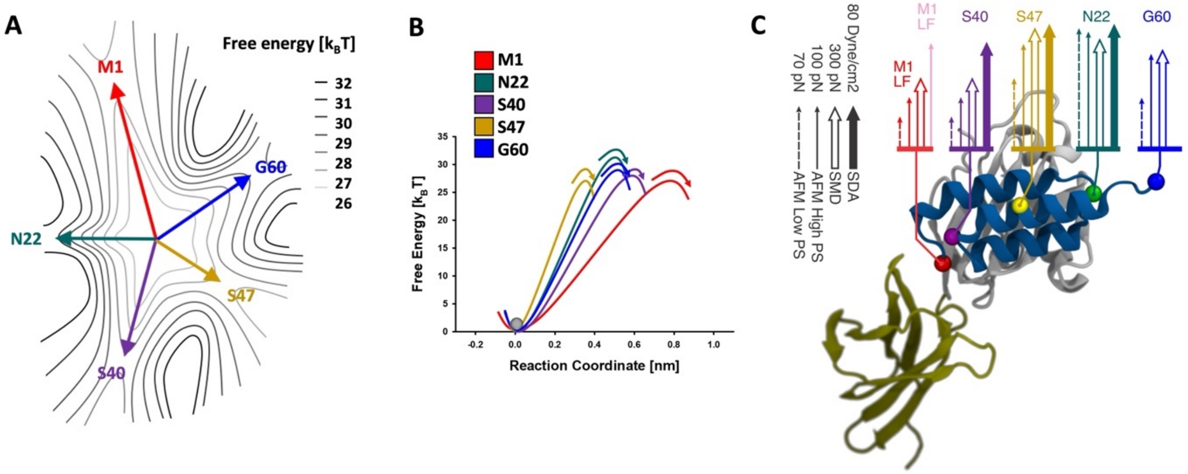

**Figure 5.** Depictions of mechanical anisotropy of the AFF:(PD-L1) complex. (A) Energy landscape with the five pulling points represented as colored arrows. (B) Unbinding energy barrier heights and barrier positions extracted from DHS model fitting for each pulling geometry. (C) Mechanical anisotropy mapped onto the AFF:(PD-L1) complex structure. The level of mechanostability is indicated by the length of arrows. Dashed arrow: rupture force from AFM-SMFS at the lowest pulling speed, 0.1x10$^3$ nm s$^{-1}$; line arrow: rupture force from AFM-SMFS at the highest pulling speed, 6.4x10$^3$ nm s$^{-1}$; open arrow: rupture force from SMD at 2.5 x 10$^9$ nm s$^{-1}$; filled arrow: $\tau_{50}$ from SDA at 4000 rpm. Quantitative scale of arrows is indicated by the black arrows on the right.

## Conclusion

We reported experimental AFM-SMFS analysis, SMD simulations and microbead adhesion assays that demonstrate how altering the surface attachment point (i.e. anchor point) can be used to modulate the mechanical stability of a therapeutic AFF:(PD-L1) complex. Our AFF scaffold is small in size with limited candidate regions eligible for pulling point insertion. We tested 5 pulling positions within AFF and found significant effects on the mechanostability of the AFF:(PD-L1) complex. Depending on the pulling point, these effects included changes in the shape of the unbinding/unfolding energy landscape, different rupture force ranges and loading rate dependencies, along with the occurrence of partially unfolded intermediate states of PD-L1, and catch bond behavior. Computational SMD simulations provided detailed molecular insight into the AFF:(PD-L1) complex with consistent tendencies in rupture force ranges as compared with experimental AFM-SMFS. Based on the parameters extracted from both experimental measurements and simulations, we depicted the energy landscape of the AFF:(PD-L1) complex dissociation reaction as a function of AFF pulling position (**Figure 5A, B**). The steep energy barrier found for N22 contributed to the highest mechanostability by AFM-SMFS analysis. The energy barrier for S47, another mechanostable pulling geometry, was not as high, but the shorter Δx made it the most mechanostable geometry at high loading rates. On the contrary, the longer Δx found for anchor points M1 and S40 made them the least resistant to external force.

We also addressed how these molecular mechanical effects could influence collective and multivalent interactions using microbead adhesion assays under shear stress. This analysis more closely represents a therapeutic or drug delivery scenario for this particular complex, where dynamic interactions and multivalency can influence the response under shear stress. The SDA analyses revealed different τ50 values from three internal pulling points which were consistent with single-molecule analysis by AFM-SMFS and SMD simulations.

We mapped the various measurement and simulation results describing the mechanostability of the AFF:(PD-L1) complex as a function of AFF pulling point onto the protein structure (**Figure 5C**). In all approaches, the analyses were generally consistent and demonstrated significant differences in mechanostability for the various anchor points. Equilibrium binding affinity meanwhile did not change upon introduction of the pulling point mutations, therefore our findings demonstrate how the mechanostability of protein complexes including therapeutic non-antibody scaffolds can be quantified and engineered by altering the loading geometry. This concept suggests that therapeutic efficacy of drug- and nanoparticle targeting proteins can potentially be improved by selecting conjugation points for payloads with optimal stability under force.

## Methods/Experimental

All experimental methods are provided in the electronic supporting information.

**Acknowledgments.** This work was supported by the University of Basel, ETH Zurich and a Consolidator Grant from the Swiss State Secretariat for Education, Research and Innovation (SERI) to MN. RCB and DEBG are supported by the National Science Foundation under Grant MCB-2143787, and the National Institute of General Medical Sciences (NIGMS) of NIH through the grant R24-GM145965. This work used SDSC's Expanse Supercomputer and NCSA's Delta Supercomputer through allocation BIO230132 from the Advanced Cyberinfrastructure Coordination Ecosystem: Services & Support (ACCESS) program, which is supported by National Science Foundation grants 2138259, 2138286, 2138307, 2137603, and 2138296.

**Competing Interests.** The authors declare no competing interests.

**Author Contributions.** B.Y. and M.A.N. conceived the study. B.Y. and Z.L. prepared biological samples. B.Y. performed AFM-SMFS and flow cytometry-based binding experiments, and analyzed the data. B.Y. and M.S.S. performed SDA experiments and analyzed the data. D.E.B.G. performed SMD simulations. R.C.B. and M.A.N. supervised the project. B.Y., D.E.B.G., and M.A.N. drafted and edited the manuscript with input from all authors. All authors reviewed the manuscript.

**Supplementary Information.** Electronic supplementary information is available for this article. This includes experimental materials and methods, protein sequences, a list of DNA primers, supplementary figures S1 – S15, and supplementary videos 1-5.

## References

1. Dietz, H., Berkemeier, F., Bertz, M. & Rief, M. Anisotropic deformation response of single protein molecules. *Proc. Natl. Acad. Sci. U. S. A.* **103**, 12724–12728 (2006).
2. Carrion-Vazquez, M. *et al.* The mechanical stability of ubiquitin is linkage dependent. *Nat. Struct. Biol.* **10**, 738–743 (2003).
3. Brockwell, D. J. *et al.* Pulling geometry defines the mechanical resistance of a beta-sheet protein. *Nat. Struct. Biol.* **10**, 731–737 (2003).
4. Cai, W. *et al.* Anisotropic Friction in a Ligand-Protein Complex. *Nano Lett.* **23**, 4111–4119 (2023).
5. Popa, I. & Berkovich, R. *Mechanical Unfolding Response of Proteins*. (American Chemical Society, 2023).
6. Kufer, S. K., Puchner, E. M., Gumpp, H., Liedl, T. & Gaub, H. E. Single-Molecule Cut-and-Paste Surface Assembly. *Science* **319**, 594–596 (2008).
7. Liu, Z. *et al.* Mapping Mechanostable Pulling Geometries of a Therapeutic Anticalin/CTLA-4 Protein Complex. *Nano Lett.* **22**, 179–187 (2022).
8. Liu, H., Liu, Z., Sá Santos, M. & Nash, M. A. Direct Comparison of Lysine versus Site-Specific Protein Surface Immobilization in Single-Molecule Mechanical Assays. *Angew. Chem. Int. Ed Engl.* **62**, e202304136 (2023).
9. Schoeler, C. *et al.* Mapping Mechanical Force Propagation through Biomolecular Complexes. *Nano Lett.* **15**, 7370–7376 (2015).
10. Sedlak, S. M. *et al.* Direction Matters: Monovalent Streptavidin/Biotin Complex under Load. *Nano Lett.* **19**, 3415–3421 (2019).
11. Sedlak, S. M., Schendel, L. C., Gaub, H. E. & Bernardi, R. C. Streptavidin/biotin: Tethering geometry defines unbinding mechanics. *Sci Adv* **6**, eaay5999 (2020).
12. Zheng, P., Chou, C.-C., Guo, Y., Wang, Y. & Li, H. Single molecule force spectroscopy reveals the molecular mechanical anisotropy of the FeS4 metal center in rubredoxin. *J. Am. Chem. Soc.* **135**, 17783–17792 (2013).
13. Qin, J. *et al.* Imaging and quantifying analysis the binding behavior of PD-L1 at molecular resolution by atomic force microscopy. *Anal. Chim. Acta* **1191**, 339281 (2022).
14. Bui, V.-C. & Nguyen, T.-H. The Role of Single-Molecule Force Spectroscopy in Unraveling Typical and Autoimmune Heparin-induced Thrombocytopenia. *Int. J. Mol. Sci.* **19**, (2018).
15. Škrlec, K., Štrukelj, B. & Berlec, A. Non-immunoglobulin scaffolds: a focus on their targets. *Trends Biotechnol.* **33**, 408–418 (2015).
16. Gebauer, M. & Skerra, A. Engineered Protein Scaffolds as Next-Generation Therapeutics. *Annu. Rev. Pharmacol. Toxicol.* **60**, 391–415 (2020).
17. Frejd, F. Y. & Kim, K.-T. Affibody molecules as engineered protein drugs. *Exp. Mol. Med.* **49**, e306 (2017).
18. Löfblom, J. *et al.* Affibody molecules: engineered proteins for therapeutic, diagnostic and biotechnological applications. *FEBS Lett.* **584**, 2670–2680 (2010).
19. Ståhl, S. *et al.* Affibody Molecules in Biotechnological and Medical Applications. *Trends Biotechnol.* **35**, 691–712 (2017).
20. Rubins, D. J. *et al.* In Vivo Evaluation and Dosimetry Estimate for a High Affinity Affibody PET Tracer Targeting PD-L1. *Mol. Imaging Biol.* **23**, 241–249 (2021).
21. González Trotter, D. E. *et al.* In Vivo Imaging of the Programmed Death Ligand 1 by F PET. *J. Nucl. Med.* **58**, 1852–1857 (2017).
22. Grindel, B. J. *et al.* Directed Evolution of PD-L1-Targeted Affibodies by mRNA Display. *ACS Chem. Biol.* **17**, 1543–1555 (2022).
23. Patel, S. P. & Kurzrock, R. PD-L1 Expression as a Predictive Biomarker in Cancer Immunotherapy. *Mol. Cancer Ther.* **14**, 847–856 (2015).

24. Goodman, A., Patel, S. P. & Kurzrock, R. PD-1-PD-L1 immune-checkpoint blockade in B-cell lymphomas. *Nat. Rev. Clin. Oncol.* **14**, 203–220 (2017).
25. Iwai, Y. *et al.* Involvement of PD-L1 on tumor cells in the escape from host immune system and tumor immunotherapy by PD-L1 blockade. *Proc. Natl. Acad. Sci. U. S. A.* **99**, 12293–12297 (2002).
26. Akinleye, A. & Rasool, Z. Immune checkpoint inhibitors of PD-L1 as cancer therapeutics. *J. Hematol. Oncol.* **12**, 92 (2019).
27. Ott, W., Jobst, M. A., Schoeler, C., Gaub, H. E. & Nash, M. A. Single-molecule force spectroscopy on polyproteins and receptor-ligand complexes: The current toolbox. *J. Struct. Biol.* **197**, 3–12 (2017).
28. Yang, B., Liu, Z., Liu, H. & Nash, M. A. Next Generation Methods for Single-molecule Force Spectroscopy on Polyproteins and Receptor-Ligand Complexes. *Frontiers in Molecular Biosciences* **7**, 85 (2020).
29. Thomas, W. E., Vogel, V. & Sokurenko, E. Biophysics of catch bonds. *Annu. Rev. Biophys.* **37**, 399–416 (2008).
30. Marshall, B. T. *et al.* Direct observation of catch bonds involving cell-adhesion molecules. *Nature* **423**, 190–193 (2003).
31. Pierse, C. A. & Dudko, O. K. Distinguishing Signatures of Multipathway Conformational Transitions. *Phys. Rev. Lett.* **118**, 088101 (2017).
32. Bizzarri, A. R. & Cannistraro, S. *Dynamic Force Spectroscopy and Biomolecular Recognition*. (CRC Press, 2012).
33. Jacobson, D. R., Uyetake, L. & Perkins, T. T. Membrane-Protein Unfolding Intermediates Detected with Enhanced Precision Using a Zigzag Force Ramp. *Biophys. J.* **118**, 667–675 (2020).
34. Milles, L. F., Schulten, K., Gaub, H. E. & Bernardi, R. C. Molecular mechanism of extreme mechanostability in a pathogen adhesin. *Science* **359**, 1527–1533 (2018).
35. Santos, M. S., Liu, H., Schittny, V., Vanella, R. & Nash, M. A. Correlating single-molecule rupture mechanics with cell population adhesion by yeast display. *Biophys Rep (N Y)* **2**, None (2022).
36. Horbett, T. A., Waldburger, J. J., Ratner, B. D. & Hoffman, A. S. Cell adhesion to a series of hydrophilic-hydrophobic copolymers studied with a spinning disc apparatus. *J. Biomed. Mater. Res.* **22**, 383–404 (1988).
37. García, A. J., Ducheyne, P. & Boettiger, D. Quantification of cell adhesion using a spinning disc device and application to surface-reactive materials. *Biomaterials* **18**, 1091–1098 (1997).
38. Kalim, M. *et al.* Construction of high level prokaryotic expression and purification system of PD-L1 extracellular domain by using Escherichia coli host cell machinery. *Immunol. Lett.* **190**, 34–41 (2017).
39. Zakeri, B. & Howarth, M. Spontaneous intermolecular amide bond formation between side chains for irreversible peptide targeting. *J. Am. Chem. Soc.* **132**, 4526–4527 (2010).
40. Zakeri, B. *et al.* Peptide tag forming a rapid covalent bond to a protein, through engineering a bacterial adhesin. *Proc. Natl. Acad. Sci. U. S. A.* **109**, E690-7 (2012).
41. Yang, B., Liu, H., Liu, Z., Doenen, R. & Nash, M. A. Influence of fluorination on single-molecule unfolding and rupture pathways of a mechanostable protein adhesion complex. *bioRxiv* (2020) doi:10.1101/2020.07.09.194894.
42. Ponnuraj, K. *et al.* A “dock, lock, and latch” structural model for a staphylococcal adhesin binding to fibrinogen. *Cell* **115**, 217–228 (2003).
43. Liu, Z. *et al.* Engineering an artificial catch bond using mechanical anisotropy. *bioRxiv* (2023) doi:10.1101/2023.09.12.557335.
44. Evans, E. & Ritchie, K. Dynamic strength of molecular adhesion bonds. *Biophys. J.* **72**, 1541–1555 (1997).
45. Bell, G. I. Models for the Specific Adhesion of Cells to Cells. *Science* **200**, 618–627 (1978).
46. Dudko, O. K., Hummer, G. & Szabo, A. Theory, analysis, and interpretation of single-molecule force

spectroscopy experiments. *Proc. Natl. Acad. Sci. U. S. A.* **105**, 15755–15760 (2008).

47. Gomes, D. E. B., Yang, B., Vanella, R., Nash, M. A. & Bernardi, R. C. Integrating Dynamic Network Analysis with AI for Enhanced Epitope Prediction in PD-L1:Affibody Interactions. *bioRxiv* (2024) doi:10.1101/2024.02.08.579577.
48. Melo, M. C. R., Bernardi, R. C., de la Fuente-Nunez, C. & Luthey-Schulten, Z. Generalized correlation-based dynamical network analysis: a new high-performance approach for identifying allosteric communications in molecular dynamics trajectories. *J. Chem. Phys.* **153**, 134104 (2020).
49. Jumper, J. *et al.* Highly accurate protein structure prediction with AlphaFold. *Nature* **596**, 583–589 (2021).
50. Evans, R. *et al.* Protein complex prediction with AlphaFold-Multimer. *bioRxiv* (2021) doi:10.1101/2021.10.04.463034.
51. Humphrey, W., Dalke, A. & Schulten, K. VMD: visual molecular dynamics. *J. Mol. Graph.* **14**, 33–8, 27–8 (1996).
52. Marru, S. *et al.* Cybershuttle: An end-to-end cyberinfrastructure continuum to accelerate discovery in science and engineering. in *Practice and Experience in Advanced Research Computing* (ACM, New York, NY, USA, 2023). doi:10.1145/3569951.3593602.
53. Strande, S. *et al.* Expanse: Computing without boundaries. in *Practice and Experience in Advanced Research Computing* (ACM, New York, NY, USA, 2021). doi:10.1145/3437359.3465588.
54. Jorgensen, W. L., Chandrasekhar, J., Madura, J. D., Impey, R. W. & Klein, M. L. Comparison of simple potential functions for simulating liquid water. *J. Chem. Phys.* **79**, 926–935 (1983).
55. Phillips, J. C. *et al.* Scalable molecular dynamics on CPU and GPU architectures with NAMD. *J. Chem. Phys.* **153**, 044130 (2020).
56. Best, R. B. *et al.* Optimization of the additive CHARMM all-atom protein force field targeting improved sampling of the backbone φ, ψ and side-chain χ(1) and χ(2) dihedral angles. *J. Chem. Theory Comput.* **8**, 3257–3273 (2012).
57. MacKerell, A. D. *et al.* All-atom empirical potential for molecular modeling and dynamics studies of proteins. *J. Phys. Chem. B* **102**, 3586–3616 (1998).
58. Darden, T., York, D. & Pedersen, L. Particle mesh Ewald: An *N*·log(*N*) method for Ewald sums in large systems. *J. Chem. Phys.* **98**, 10089–10092 (1993).
59. Phillips, J. C. *et al.* Scalable molecular dynamics with NAMD. *J. Comput. Chem.* **26**, 1781–1802 (2005).
60. Hunter, J. D. Matplotlib: A 2D Graphics Environment. *Comput. Sci. Eng.* **9**, 90–95 (2007).
61. The pandas development team. *Pandas-Dev/Pandas: Pandas*. (Zenodo, 2024). doi:10.5281/ZENODO.3509134.
62. Waskom, M. seaborn: statistical data visualization. *J. Open Source Softw.* **6**, 3021 (2021).

# Supporting Information

# Engineering the Mechanical Stability of a Therapeutic Complex between Affibody and Programmed Death-Ligand 1 by Anchor Point Selection

Byeongseon Yang[1,2,*], Diego E. B. Gomes[3,*], Zhaowei Liu[1,2,4], Mariana Sá Santos[1,2], Jiajun Li[1,2],
Rafael C. Bernardi[3,§], and Michael A. Nash[1,2,§]

[1] Institute for Physical Chemistry, Department of Chemistry, University of Basel, 4058 Basel, Switzerland
[2] Department of Biosystems Science and Engineering, ETH Zurich, 4058 Basel, Switzerland
[3] Department of Physics, Auburn University, Auburn, Alabama 36849, United States
[4] Present address: Department of Bionanoscience, Delft University of Technology, 2629HZ Delft, the Netherlands

* These authors contributed equally to the study

§ Correspondence to: rcbernardi@auburn.edu; michael.nash@unibas.ch

# Materials & Methods

### Plasmids available on addgene:

Addgene plasmid #157674: pET28a-ybbR-His-ELP(MV7E2)3-FLN-SpyCatcher

### Cloning of PD-L1-ECD-HIS and PD-L1-ECD-HIS-SpyTag

DNA sequence of extracellular domain of human PD-L1 was chemically synthesized based on the codon usage of E. coli (GeneArt, Thermo Fisher Scientific) and introduced into pET28a vector via NdeI and XhoI restriction sites generating a new vector pET28a-PD-L1-ECD-HIS, confirmed by further DNA sequencing analysis.

For the AFM-SMFS analysis, SpyTag was further introduced at the C-terminus of PD-L1 by PCR using primer #1 and #2 (Table S1) based on the plasmid pET28a-PD-L1-ECD-HIS and following Gibson assembly with master mix (NEB) generating a new vector pET28a-PD-L1-ECD-HIS-SpyTag, which was confirmed by further DNA sequencing analysis.

### Cloning of AFF-HIS, Fgβ-AFF-HIS, AFF-N-TAG-HIS (M1), AFF-N22TAG-HIS (N22), AFF-S40TAG-HIS (S40), AFF-S47TAG-HIS (S47), and AFF-C-TAG-HIS (G60)

DNA sequence of Anti-PD-L1 Affibody (AFF) was chemically synthesized based on the codon usage of E. coli (GeneArt, Thermo Fisher Scientific) and introduced into pET28a vector via NdeI and XhoI restriction sites generating a new vector pET28a-Anti-PD-L1-AFF-HIS (for preparation of AFF-HIS), which was confirmed by further DNA sequencing analysis.

For the AFM-SMFS analysis, Fgβ was further introduced at the N-terminus of AFF by PCR using primer #3 and #4 (Table S1) based on the plasmid pET28a-Anti-PD-L1-AFF-HIS and following Gibson assembly with master mix (NEB) generating a new vector pET28a-Fgβ-Anti-PD-L1-AFF-HIS, which was confirmed by further DNA sequencing analysis.

For the incorporation of pAzF into AFF, five different positions were decided (M1, N22, S40, S47, and G60) and amber codon was introduced at each position by site directed mutagenesis using the Q5® Site-Directed Mutagenesis kit (NEB) with primer #5 and #6 for M1, primer #7 and #8 for N22, primer #9 and #10 for S40, primer #11 and #12 for S47, and primer #13 and #14 for G60 (Table S1), generating new plasmids pET28a-Anti-PD-L1-AFF-N-TAG-HIS, pET28a-Anti-PD-L1-AFF-N22TAG-HIS, pET28a-Anti-PD-L1-AFF-S40TAG-HIS, pET28a-Anti-PD-L1-AFF-S47TAG-HIS, and pET28a-Anti-PD-L1-AFF-C-TAG-HIS, which was confirmed by further DNA sequencing analysis.

### Expression, Refolding, and Purification of PD-L1 Variants

The plasmid with the sequence of PD-L1 variants was introduced into competent E. coli BL21(DE3) strain. Recombinant cells were cultured in 5 ml of Luria-Bertani (LB) medium with 50 µg ml-1 kanamycin at 37 °C overnight. The culture was transferred to 50 mL of Terrific broth (TB) medium with 50 µg ml-1 kanamycin and cultivated at 37 °C and 200 rpm until an optical density at 600 nm (OD600) of ~0.8-1.0 was reached. The expression of recombinant protein was induced by the addition of 1.0 mM isopropyl-β-D-thio-galactopyranoside (IPTG) and the culture was further incubated at 37 °C and 200 rpm for ~9 hrs. The cells were harvested by centrifugation at 4,000 g for 20 min at 4 °C.

The harvested cell pellet was resuspended in a denaturing lysis buffer (10 mM Tris-Cl, and 8M urea; pH ~8). Resuspended cells were placed on ice and disrupted for 15 min using a sonic dismembrator using a 3 s on: 5 s off pattern to allow cooling between each pulse. The lysate was centrifuged at 14,000 g for 20 min at 4 °C. The supernatant was collected and incubated with Ni-NTA resin for 30 min at room temperature to allow the His6-tagged proteins to bind to the Ni-NTA resin. Then, the mixture was loaded onto a column. The resin was washed with 10–20 resin volumes of wash buffer (20 mM imidazole, 10 mM Tris-Cl, and 8M urea; pH ~8). Recombinant proteins were eluted in the elution buffer (500 mM imidazole, 10 mM Tris-Cl, and 8M urea; pH ~8). The eluted protein solution was serially dialyzed to 8 M, 4 M, 2 M, and 0 M Urea with 5% glycerol, 5% sucrose, 1% arginine, 0.5 mM NaCl in 20 mM Tris-Cl (pH 7.4), and finally to 1x PBS buffer. Precipitation during dialysis was removed by centrifugation at 14,000 g for 20 min at 4 °C and supernatant was further purified by SEC column.

### Expression and Purification of AFF Variants

The plasmid with the sequence of AFF variants was introduced into a competent E. coli BL21(DE3) strain. Recombinant cells were cultured in 5 ml of Luria-Bertani (LB) medium with 50 µg ml-1 kanamycin at 37 °C overnight. The culture was transferred to 50 mL of Terrific broth (TB) medium with 50 µg ml-1 kanamycin and cultivated at 37 °C and 200 rpm until an optical density at 600 nm (OD600) of ~0.8-1.0 was reached. The expression of recombinant protein was induced by the addition of 1.0 mM isopropyl-β-D-thio-galactopyranoside (IPTG) and the culture was further incubated at 37 °C and 200 rpm for ~9 hrs. The cells were harvested by centrifugation at 4,000 g for 20 min at 4 °C. The cells were harvested by centrifugation at 4,000 g for 20 min at 4 °C. The harvested cell pellet was resuspended in lysis buffer (50 mM Tris, 50 mM NaCl, 0.1% Triton X-100, 5 mM MgCl2; pH 8.0), and disrupted with a sonic dismembrator. The lysate was centrifuged at 14,000 g for 20 min at 4 °C. The supernatant was collected and incubated with Ni-NTA resin, loaded onto a column, washed with wash buffer (1x PBS with 20 mM imidazole; pH 7.4), and eluted in elution buffer (1x PBS with 500 mM imidazole; pH 7.4). The eluted protein solution was further purified by the SEC column.

### Amber Suppression

Five AFF variants for the free diffusion system of AFM-SMFS analysis were prepared by site-specific incorporation of p-azido-l-phenylalanine (pAzF) at each pulling point using the amber suppression method. The plasmid with the sequence of AFF variants was co-introduced into competent E. coli BL21(DE3) strain with the plasmid pEVOL-pAzF (addgene #31186). The cell culture was transferred to 100 mL of Luria-Bertani (LB) medium with 50 µg ml-1 kanamycin and 34 µg mL-1 chloramphenicol and cultivated at 37 °C and 200 rpm until an optical density at 600 nm (OD600) of ~0.8-1.0 was reached. Then, the cells were collected, washed with ice-cold 0.9% NaCl twice, and transferred to 100 mL M9 medium supplemented with 50 µg mL-1 kanamycin, 34 µg mL-1 chloramphenicol, 1 mM pAzF and 0.02% arabinose. The culture was incubated at 37 °C for 1 h and the expression of recombinant protein was induced by the addition of 1.0 mM IPTG and the culture was further incubated at 20 °C and 200 rpm overnight. Purification of the protein was carried out in the same manner as illustrated previously.

### Conjugation of Fgβ peptide to AFF

Fgβ-StrepTag-DBCO peptide (JPT Peptide Technologies GmbH, Berlin, Germany) was added to pAzF-incorporated AFF with a molar ratio of 3:1. The mixture was incubated at room temperature with shaking for 1 h, followed by incubation at 4 °C overnight. Successful conjugation was confirmed by SDS-PAGE analysis and conjugated AFF was further purified with SEC in 1x PBS buffer to remove the excess peptide.

### High-resolution mass spectrometry

Purified AFF variants and Fgβ-conjugated AFF variants protein solution was desalted using Zeba$^{TM}$ spin desalting column (Thermo Fisher Scientific) and diluted to a concentration of 0.2-1.0 mg mL-1 with a final concentration of 0.1% formic acid. The separation of the sample protein analytes was carried out using an UltiMate™ 3000 UHPLC-system equipped with 50 mm Phenomenex Jupiter C4 column (Thermo Fischer Scientific) with a diameter of 2.0 mm, 300 Å pore size, and 5 µm particle size. 1 µL of protein solution was injected for all analyses and the column was kept at 30 °C. HRMS-spectra were acquired on a Bruker maXis

4G ESI-QTOF (Bruker Daltonics) and data deconvolution was done with Bruker Compass DataAnalysis 4.4.

**Surface preparation and protein immobilization for AFM-SMFS**

The surface modification of cantilever and coverglasses and the protein immobilization were done in the same manner as previously illustrated (Figure 1D). Cantilevers were cleaned by UV-ozone treatment for 40 min and cover glasses were soaked in piranha etching solution and rinsed with distilled water (DW). Then, cantilevers and coverglasses were treated with 3-Aminopropyl (diethoxy) methylsilane (APDMES, ABCR GmbH, Karlsruhe, Germany) to silanize the surfaces with amine groups. The amine groups subsequently reacted to a NHS group from sulfosuccinimidyl 4-(N-maleimidomethyl)cyclohexane-1-carboxylate (sulfo-SMCC; Thermo Fischer Scientific) in 50 mM HEPES buffer pH 7.5 for 30 min. The thiol group from Coenzyme A (CoA, 200 µM) reacted to a maleimide group from sulfo-SMCC in coupling buffer (50 mM sodium phosphate, 50 mM NaCl, 10 mM EDTA, pH 7.2) for 2 hrs. Finally, the ybbR-tagged proteins SdrG-FLN-ELP-His-ybbR and pre-conjugated ybbR-His-ELP-FLN-SpyCatcher:PD-L1-SpyTag were site-specifically anchored to the surface using SFP-mediated ligation to CoA in $Mg^{2+}$ supplemented 1x PBS buffer. This resulted in covalent immobilization of SdrG and PD-L1 to cantilever and cover glasses, respectively. Protein-immobilized cantilevers and coverglasses were extensively washed and kept in 1x PBS buffer prior to immediate use. SpyTag-SpyCatcher conjugation of ybbR-His-ELP-FLN-SpyCatcher and PD-L1-ECD-HIS-SpyTag was done by mixing two proteins with the same molar ratio in 1x PBS buffer and pre-incubation for 1 hr prior to ybbR tag ligation.

**AFM-SMFS measurement and data analysis**

Force spectroscopy measurements of PD-L1 and AFF with different pulling geometry were conducted in the same manner as previously illustrated using automated AFM-based SMFS (Force Robot 300, JPK Instruments) with free-diffusion system via SdrG handle. ~ 1 µM of each Fgβ-conjugated AFF variant was added to the measurement buffer between PD-L1 immobilized coverglass and SdrG immobilized cantilever. After mounting the samples and cantilever with equilibrium time of 30-60 min, spring constant of the cantilever (0.02-0.14 N $m^{-1}$) and detector sensitivity were calibrated using the contact-free mode. SMFS data were recorded in 1x PBS buffer at room temperature with constant pulling speed mode. The cantilever was approached to the glass surface, dwelled for 200 ms and retracted at constant pulling speeds of $0.1x10^3$, $0.4x10^3$, $1.6x10^3$, $6.4x10^3$ nm $s^{-1}$. Force-extension curves were acquired, filtered and analyzed by a combination of software available on the AFM instrument (JPK SPM Data Processing software) and custom python scripts. Exported force-extension curves were transformed to contour length ($L$) using the worm like chain (WLC) mode described by Eq. (1) (ref: 63):

$$L = \frac{x}{6u}\left(3 + 4u + \frac{9-3+4u^2}{g(u)} + g(u)\right) \tag{1}$$

where $g(u) = \left(27 - \frac{27u}{2} + 36u^2 - 8u^3 + \frac{3\sqrt{3}}{2}\sqrt{-u^2[(4u-3)^3 - 108]}\right)^{\frac{1}{3}}$ , $u = \frac{Fp}{k_B T}$, Boltzmann's constant $k_B T$, distance $x$ with fixed persistence length $p = 0.4\,nm$, and temperature $T = 22$ °C for the calculation. The data traces were filtered by searching for contour length increments that matched the lengths of the fingerprint domains, FLN (≈36 nm). Theoretical contour length increment was calculated based on the equation ΔLc = (0.365 nm/AA) × (# AAs in POI) - Lf, where ΔLc is expected contour length increment and Lf is end-to-end length of folded protein domain. For FLN, ΔLc = 36.9 nm - Lf, where Lf is typically < 5nm. For the Fgβ-AFF (N-terminal pulling geometry), final rupture force was not significantly strong enough to unfold fingerprint domain FLN. Therefore, data traces without FLN unfolding were also selected. The loading rate values were extracted from the slope of the force vs time trace very close (~2nm) prior to the rupture peak. For dynamic force spectra, the rupture or unfolding forces vs. loading rate was plotted and median forces and loading rates for each pulling speed were fitted to Bell-Evans model to estimate the effective distance to the transition state (Δx) and the intrinsic dissociation rate or unfolding rate (koff) in the absence of force. For the Dudko–Hummer–Szabo model fitting (ref: 46, 64), histograms of the rupture force of the complex were plotted using equal bin with $\Delta F$ = 10 pN for M1 LF and S40 and $\Delta F$ = 20 pN for M1 HF, N22, S47, and G60. For one histogram containing $N$ bins, starting from $F_0$ and ending at $F_N = F_0 + N\Delta F$, the $k$th bin can be directly transformed into the force-dependent rate constant value using Eq. (2):

$$k_{off}(F_k) = \frac{h_k r(F_k)}{\left(\frac{h_k}{2} + \sum_{i=k+1}^{N} h_i\right)\Delta F} \tag{2}$$

where $k_{off}(F_k)$ is the off rate under the average rupture force of the $k$th bin, $r(F_k)$ is the average loading rate of the $k$th bin, and $h_k$ is the height of the $k$th bin, which is calculated using Eq. (3):

$$h_k = \frac{C_k}{C_{tot}\Delta F} \tag{3}$$

where $C_k$ is the number of counts in the $k$th bin and $C_{tot}$ is the total number of counts from the histogram. The force-dependence of $k_{off}(F)$ can be described based on Kramers theory as Eq. (4):

$$k_{off}(F) = k_0 \left(1 - \frac{vF\Delta x^{\ddagger}}{\Delta G^{\ddagger}}\right)^{\frac{1}{v}-1} e^{\beta\Delta G^{\ddagger}\left[1-\left(1-\frac{vF\Delta x^{\ddagger}}{\Delta G^{\ddagger}}\right)^{\frac{1}{v}}\right]} \tag{4}$$

where $k_0$ is the intrinsic off rate in the absence of force, $\Delta x^{\ddagger}$ is the distance to the energy barrier, $\Delta G^{\ddagger}$ is the height of the energy barrier in the absence of force, $\beta^{-1} = k_B T$, and $v$ = ½ or 2/3 depending on the assumption of the free-energy surface shape to cusp or linear-cubic, respectively. Therefore, the effective distance to the transition state (Δx), the intrinsic dissociation rate (koff) in the absence of force, and the height of the energy barrier (ΔG) were estimated by fitting Eq. (4) on the $logk_{off}$-Force plot. The asymptotic expressions for the mean rupture force and variance from Eq. (4) can be further described as Eq. (5):

$$\langle F \rangle \cong \frac{\Delta G^{\ddagger}}{vx^{\ddagger}}\left\{1 - \left[\frac{1}{\Delta G^{\ddagger}} ln \frac{k_0 e^{\Delta G^{\ddagger}+\gamma}}{x^{\ddagger}KV}\right]^{v}\right\} \tag{5}$$

where $KV$ is the loading rate and the Euler-Mascheroni constant $\gamma$ = 0.577. The rupture force and loading rate values from the dynamic force spectra with multiple pulling speeds were fitted to Eq. (5) on the force-distance curves.

## Conjugation of FAM to AFF

Fluorescent dye-conjugated AFF solution was prepared by DBCO-azide click chemistry between DBCO-PEG4-FAM5/6 (Jena Bioscience) and pAzF-incorporated AFFs with different 5 positions (AFF-N-pAzF, AFF-N22pAzF, AFF-S40pAzF, AFF-S47pAzF, AFF-C-pAzF). DBCO-PEG4-FAM5/6 was added to pAzF-incorporated AFFs with a molar ratio of 5:1. The mixture was incubated at room temperature with shaking for 1 h, followed by incubation at 4 °C overnight. Unreacted FAM molecules were removed by further purification via His6x-tag and Ni-NTA resin. Successful conjugation was confirmed by SDS-PAGE analysis and conjugated AFF was further purified with SEC in 1x PBS buffer.

## Binding affinity analysis based on flow cytometry

The binding affinity between AFF variants and PD-L1 was measured using the Attune NxT (Thermo Fisher

Scientific) flow cytometer equipped with a 488 nm and a 561 nm laser. First, SpyCatcher was immobilized onto the surface of amine-functionalized PS beads via ybbR Tag. Then, SpyCatcher-immobilized PS bead was incubated with 10 µM PD-L1-SpyTag solution for > ~2 hrs at RT to conjugate PD-L1 to PS bead by isopeptide bond formation between SpyTag and SpyCatcher. PD-L1 immobilized beads were incubated in FAM-labeled AFF variants' solution with different concentrations ranging from 0.04 nM to 625 nM for ~1-2 hrs at RT. After washing, shift of fluorescence from FAM was recorded and plotted against the concentration of AFF to derive the dissociation constant between PD-L1-S and AFFs with different conjugation geometry.

## Computational models

The initial model was obtained previously described[47]. Briefly, the sequences for the mature domain of PD-L1 (UniProt Q9NZQ7, 18-234) and the Affibody (1-60) were used as input for prediction using AlphaFold version 2.3.2[49,50] in multimer mode using all 5 available v3 multimer parameter sets, resulting in a total of 25 predictions per sequence pair. The QwikFold VMD's[51] plugin was used to set the experiments and post-process the results, and calculations were run using the Cybershuttle[52] Research Environment deployed at the SDSC Expanse[53] supercomputer and at NCSA's Delta Supercomputer.

### *Molecular dynamics (MD) simulation*

The (PD-L1):AFFibody were subjected to refinement and conformational sampling by molecular dynamics simulations. The system was then solvated with TIP3P[54] water and neutralized using Sodium atoms as counter-ions, which were randomly arranged in the solvent. Total system sizes were approximately 100k-125k atoms. The MD simulations were performed employing the GPU-accelerated molecular dynamics package NAMD3[55]. The CHARMM36 force field [56,57] was used to describe all systems. The simulations were carried out assuming periodic boundary conditions in the NpT ensemble with temperature maintained at 300 K using Langevin dynamics for pressure, kept at 1 bar, and temperature coupling. A distance cut-off of 12.0 Å was applied to short-range, non-bonded interactions, whereas long-range electrostatic interactions were treated using the particle-mesh Ewald (PME)[58] method. The equations of motion were integrated using the r-RESPA multiple time step scheme[59] to update the van der Waals interactions every step and electrostatic interactions every two steps. The time step of integration was chosen to be 4 fs for all simulations performed. Before the production SMD simulations all the systems were submitted to an energy minimization protocol for 5,000 steps followed by MD simulations with position restraints in the protein backbone atoms were performed for 1.0 ns, progressively raising the temperature from 10K to 300K. These steps were followed by an unrestrained equilibration for additional 5 ns.

### *Steered molecular dynamics (SMD) simulation*

In all simulations, totaling over 300 SMD simulations, SMD was employed by harmonically restraining the position of a C-terminal amino acid residue of PD-L1, and moving a second restraint point at constant speed ($2.5\text{x}10^7$ , $2.5\text{x}10^8$, $2.5\text{x}10^9$ nm $s^{-1}$) from each pulling point (Affibody residues M1, N22, S40, S47, and G60), with and extension between 6 (N22, S40, S47) and 10 ($C_{\text{terminal}}$,$N_{\text{terminal}}$) nanometers, in 40-48 production SMD runs.

### *Molecular Dynamics Simulations Analysis*

All analyses of MD trajectories were carried out employing VMD, its plugins and TCL scripts, unless stated differently. Analysis outputs were post-processed to generate graphs using Python3 libraries, including Matplotlib[60], Pandas[61], and Seaborn[62], unless stated differently. Figure panels were assembled with CorelDraw Graphics Suite 2021.

## Cys-SpyCatcher preparation

Cys-SpyCatcher protein was designed to conjugate AFF variants via maleimide-thiol reaction so that AFF variants can have the same ELP linker for spinning disk assay to SMFS analysis. In Cys-SpyCatcher protein construct, native cysteine in FLN was removed and new cysteine was introduced into the short linker region between ddFLN4 and SpyCatcher. This new DNA sequence was amplified via PCR using primer #15 and #16 (Table S1) using the plasmid #157674 (Addgene).

This PCR-amplified DNA string was assembled with PCR-amplified DNA backbone (via PCR using primers #17 and #18 (Table S1) using the plasmid #157674 (Addgene)) into a new vector pET28a-ybbR-HIS-ELP-ddFLN4-Cys-SpyCatcher using Gibson assembly master mix (NEB) and was confirmed by DNA sequencing.

Newly constructed recombinant plasmid pET28a-ybbR-HIS-ELP-ddFLN4-Cys-SpyCatcher was introduced into a competent E. coli BL21(DE3) strain. Recombinant cells were cultured in 5 ml of Luria-Bertani (LB) medium with 50 µg ml-1 kanamycin at 37 °C overnight. The culture was transferred to 50 mL of LB medium with 50 µg ml-1 kanamycin and cultivated at 37 °C and 200 rpm until an optical density at 600 nm (OD600) of ~0.7 was reached. Then, the expression was induced by the addition of 0.5 mM IPTG and the culture was further incubated at 20 °C and 200 rpm for ~18 hrs. The cells were harvested by centrifugation at 4,000 g for 20 min at 4 °C. The harvested cell pellet was resuspended in lysis buffer (50 mM Tris, 50 mM NaCl, 0.1% Triton X-100, 5 mM MgCl2; pH 8.0). Resuspended cells were placed on ice and disrupted for 15 min using a sonic dismembrator using a 3 s on: 5 s off pattern to allow cooling between each pulse. The lysate was centrifuged at 14,000 g for 20 min at 4 °C. The supernatant was collected and incubated with Ni-NTA resin for 30 min at room temperature to allow the His6x-tagged proteins to bind to the Ni-NTA resin. Then, the mixture was loaded onto a column. The resin was washed with 10–20 resin volumes of wash buffer (20 mM imidazole in 1x PBS). Recombinant proteins were eluted in the elution buffer (500 mM imidazole in 1x PBS). The eluted protein solution was directly treated with DTT and further purified by the SEC column.

### Conjugation of Cys-SpyCatcher to AFF

Cys-SpyCatcher was DBCO-functionalized using DBCO-PEG4-maleimide (BroadPharm) with reaction between free thiol of Cys-SpyCatcher and maleimide group. SEC-purified Cys-SpyCatcher after DTT treatment was mixed to DBCO-PEG4-maleimide with a ratio of ~1:15-20 at 4 °C, overnight. The following day, DBCO-functionalized Cys-SpyCatcher was purified by the SEC column. After that, AFF variants, AFF-N22pAzF, AFF-S40pAzF, and AFF-S47pAzF, were conjugated to DBCO-Cys-SpyCatcher by mixing between them with a ratio of 1:3 at 4 °C, overnight. Finally, further SEC purification resulted in AFF-pAzF-DBCO-Cys-SpyCatcher variants stock solution.

### Spinning disk assay (SDA) analysis

The surface modification of coverglasses and the protein immobilization were done in the same manner as previously illustrated. The amine groups of aminosilanized cover glasses reacted to a NHS group from sulfo-SMCC (Thermo Fischer Scientific) in 50 mM HEPES buffer pH 7.5 for 30 min. The thiol group from Coenzyme A (CoA, 200 µM) reacted to a maleimide group from sulfo-SMCC in coupling buffer (50 mM sodium phosphate, 50 mM NaCl, 10 mM EDTA, pH 7.2) for 2 hrs. Finally, each ybbR-tagged AFF-pAzF-DBCO-Cys-SpyCatcher protein variants (AFF-N22pAzF, AFF-S40pAzF, and AFF-S47pAzF) were site-specifically anchored to the surface using SFP-mediated ligation to CoA in Mg2+ supplemented 1x PBS buffer for 2 hrs. This resulted in covalent immobilization of AFF-pAzF-DBCO-Cys-SpyCatcher protein variants to cover glasses for SDA. To reduce the non-specific interaction, protein-immobilized coverglasses were treated with 5% BSA solution for 10 min. The surface modification of PS beads and the PD-L1 immobilization were also done in the same manner.

Then, PD-L1 immobilized PS beads were seeded on the surface in 1x PBS containing 0.1% BSA and allowed to adhere for 30 min at room temperature. Before spinning, the bead suspension was removed and gently replaced with PBS. The coverglasses were mounted on the spinning disk device, secured by vacuum suction, and immersed in a solution of PBS at room temperature. The coverglasses were spun with speeds of 2000 rpm and 4000 rpm for 5 min, imaged by frame at 10× magnification on an Olympus IX81 microscope (~500 individual images automatically stitched together with CellSens software (version 1.16; Olympus, Tokyo, Japan)), and saved. Taken images were further analyzed as illustrated previously with a custom Python-based image analysis script and MATLAB 2022b (The MathWorks, Natick, MA) to extract the fraction of adherent beads at different positions on the disk by normalizing the density of beads at each section of the disk with the density of beads at the center of the disk, where the shear forces are close to zero.[35] The fraction of adherent beads (f) was plotted along with the shear stress ($\tau$; Pa) and fitted to a sigmoid probabilistic model:

$$f = \frac{a}{1 + e^{b(\tau - \tau_{50})}}$$

to extract $\tau_{50}$ value which is the shear stress at which 50% of the beads remain adherent.

## Protein Sequences

**PD-L1-ECD-HIS**

MFTVTVPKDLYVVEYGSNMTIECKFPVEKQLDLAALIVYWEMEDKNIIQFVHGEEDLKVQHSSYRQRARLLKDQLSLGNAALQITDVKLQDAGVYRCMISYGGADYKRITVKVNAPYNKINQRILVVDPVTSEHELTCQAEGYPKAEVIWTSSDHQVLSGKTTTTNSKREEKLFNVTSTLRINTTTNEIFYCTFRRLDPEENHTAELVIPELPLAHPPNERGSHHHHHH

**PD-L1-ECD-HIS-SpyTag**

MFTVTVPKDLYVVEYGSNMTIECKFPVEKQLDLAALIVYWEMEDKNIIQFVHGEEDLKVQHSSYRQRARLLKDQLSLGNAALQITDVKLQDAGVYRCMISYGGADYKRITVKVNAPYNKINQRILVVDPVTSEHELTCQAEGYPKAEVIWTSSDHQVLSGKTTTTNSKREEKLFNVTSTLRINTTTNEIFYCTFRRLDPEENHTAELVIPELPLAHPPNERGSHHHHHHGSAHIVMVDAYKPTK

**AFF-HIS**

MVDAKYAKERNKAAYEILYLPNLTNAQKWAFIWKLDDDPSQSSELLSEAKKLNDSQAPKGSHHHHHH

**Fgβ-AFF-HIS**

MNEEGFFSARGHRPLDGSGSVDAKYAKERNKAAYEILYLPNLTNAQKWAFIWKLDDDPSQSSELLSEAKKLNDSQAPKGSHHHHHH

**AFF-N-TAG-HIS (M1)**

MGSGSGS-pAzF-VDAKYAKERNKAAYEILYLPNLTNAQKWAFIWKLDDDPSQSSELLSEAKKLNDSQAPKGSHHHHHH

**AFF-N22TAG-HIS (N22)**

MVDAKYAKERNKAAYEILYLP-pAzF-LTNAQKWAFIWKLDDDPSQSSELLSEAKKLNDSQAPKGSHHHHHH

**AFF-S40TAG-HIS (S40)**

MVDAKYAKERNKAAYEILYLPNLTNAQKWAFIWKLDDDP-pAzF-QSSELLSEAKKLNDSQAPKGSHHHHHH

**AFF-S47TAG-HIS (S47)**

MVDAKYAKERNKAAYEILYLPNLTNAQKWAFIWKLDDDPSQSSELL-pAzF-
EAKKLNDSQAPKGSHHHHHH

**AFF-C-TAG-HIS (G60)**

MVDAKYAKERNKAAYEILYLPNLTNAQKWAFIWKLDDDPSQSSELLSEAKKLNDSQAPKGS-pAzF-
GSGSHHHHHH

**SdrG-FLN-ELP-HIS-ybbR**

MGTEQGSNVNHLIKVTDQSITEGYDDSDGIIKAHDAENLIYDVTFEVDDKVKSGDTMTVNIDKNTVPSDLT
DSFAIPKIKDNSGEIIATGTYDNTNKQITYTFTDYVDKYENIKAHLKLTSYIDKSKVPNNNTKLDVEYKTALSS
VNKTITVEYQKPNENRTANLQSMFTNIDTKNHTVEQTIYINPLRYSAKETNVNISGNGDEGSTIIDDSTIIKVY
KVGDNQNLPDSNRIYDYSEYEDVTNDDYAQLGNNNDVNINFGNIDSPYIIKVISKYDPNKDDYTTIQQTVT
MQTTINEYTGEFRTASYDNTIAFSTSSGQGQGDLPPEGSGSGSGSADPEKSYAEGPGLDGGECFQPSK
FKIHAVDPDGVHRTDGGDGFVVTIEGPAPVDPVMVDNGDGTYDVEFEPKEAGDYVINLTLDGDNVNGFP
KTVTVKPAPGSGSGSHGVGVPGMGVPGVGVPGVGVPGVGVPGVGVPGVGVPGVGVPGVGVPGEGVP
GEGVPGVGVPGMGVPGVGVPGVGVPGVGVPGVGVPGVGVPGVGVPGVGVPGEGVPGEGVPGVGVP
GMGVPGVGVPGVGVPGVGVPGVGVPGVGVPGVGVPGVGVPGEGVPGEGVPGWRGHHHHHHGSDSL
EFIASKLA

**ybbR-HIS-ELP-FLN-SpyCatcher**

MGTDSLEFIASKLAHHHHHHWGSGHGVGVPGMGVPGVGVPGVGVPGVGVPGVGVPGVGVPGVGVPG
VGVPGEGVPGEGVPGVGVPGMGVPGVGVPGVGVPGVGVPGVGVPGVGVPGVGVPGVGVPGEGVPG
EGVPGVGVPGMGVPGVGVPGVGVPGVGVPGVGVPGVGVPGVGVPGVGVPGEGVPGEGVPGWPSGS
ADPEKSYAEGPGLDGGECFQPSKFKIHAVDPDGVHRTDGGDGFVVTIEGPAPVDPVMVDNGDGTYDVE
FEPKEAGDYVINLTLDGDNVNGFPKTVTVKPAPGSGSGSGSVDTLSGLSSEQGQSGDMTIEEDSATHIKF
SKRDEDGKELAGATMELRDSSGKTISTWISDGQVKDFYLYPGKYTFVETAAPDGYEVATAITFTVNEQGQ
VTVNGKATKGDAHI

**ybbR-HIS-ELP-FLN-Cys-SpyCatcher**

MGTDSLEFIASKLAHHHHHHWGSGHGVGVPGMGVPGVGVPGVGVPGVGVPGVGVPGVGVPGVGVPG
VGVPGEGVPGEGVPGVGVPGMGVPGVGVPGVGVPGVGVPGVGVPGVGVPGVGVPGVGVPGEGVPG
EGVPGVGVPGMGVPGVGVPGVGVPGVGVPGVGVPGVGVPGVGVPGVGVPGEGVPGEGVPGWPSGS
ADPEKSYAEGPGLDGGESFQPSKFKIHAVDPDGVHRTDGGDGFVVTIEGPAPVDPVMVDNGDGTYDVE
FEPKEAGDYVINLTLDGDNVNGFPKTVTVKPAPGSGSGCGSVDTLSGLSSEQGQSGDMTIEEDSATHIKF
SKRDEDGKELAGATMELRDSSGKTISTWISDGQVKDFYLYPGKYTFVETAAPDGYEVATAITFTVNEQGQ
VTVNGKATKGDAHI

# Supporting Figures & Tables

**Table S1.** Primers

| **Number** | **Sequence** |
|---|---|
| 1 | 5'-GTCATGGTTGATGCATACAAGCCGACGAAGTAACTCGAGTAAGATCCGGCTG-3' |
| 2 | 5'-GGCTTGTATGCATCAACCATGACAATATGGGCGCTACCGTGATGATGATGGTGATGGCTAC-3' |
| 3 | 5'-GCTGGATGGTAGCGGTAGCGTGGACGCCAAATATGCCAAAG-3' |
| 4 | 5'-GCTACCGCTACCATCCAGCGGACGATGACCACGTGCGCTAAAAAAGCCTTCTTCATTCATATGTATATCTCCTTCTTAAAGTTAAAC-3' |
| 5 | 5'-AGCGGCTCTGGTAGCTAGGTGGACGCCAAATATGCCAAAG-3' |
| 6 | 5'-GCTACCAGAGCCGCTACCCATATGTATATCTCCTTCTTAAAGTTAAAC-3' |
| 7 | 5'-GTATCTGCCGTAGCTGACCAATG-3' |
| 8 | 5'-AGAATTTCGTAGGCTGCTTTATTAC-3' |
| 9 | 5'-TGATGATCCGTAGCAGAGCAGCGAAC-3' |
| 10 | 5'-TCCAGTTTCCAGATAAATG-3' |
| 11 | 5'-CGAACTGCTGTAGGAAGCAAAAAAACTGAATGATAGCC-3' |
| 12 | 5'-CTGCTCTGGCTCGGATCA-3' |
| 13 | 5'-CTAGGGCTCTGGTAGCCATCACCATCATCATCAT-3' |
| 14 | 5'-GCTACCAGAGCCCTAGCTACCTTTCGGTGCCTGG-3' |
| 15 | 5'-AGCTTCCAGCCGTCTAAATTCAAA-3' |
| 16 | 5'-TCAGGGTATCAACGCTACCGCAACCAGAACCGGAGCCCG-3' |
| 17 | 5'-GGTAGCGTTGATACCCTGAGC-3' |
| 18 | 5'-AATTTAGACGGCTGGAAGCTTTCACCACCGTCCAGACCC-3' |

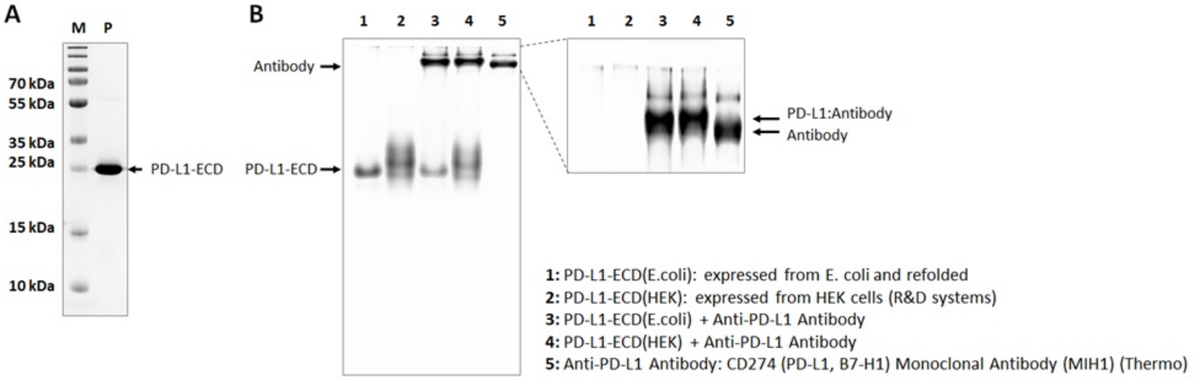

**Figure S1.** Successful expression, refolding, and purification of PD-L1-ECD from E. coli expression system. (A) SDS-PAGE analysis of purified PD-L1-ECD. (B) Native PAGE analysis of purified PD-L1-ECD and its successful binding by anti-PD-L1 antibody which is comparable to binding behavior between commercial recombinant PD-L1-ECD (from HEK cell expression system) and anti-PD-L1 antibody.

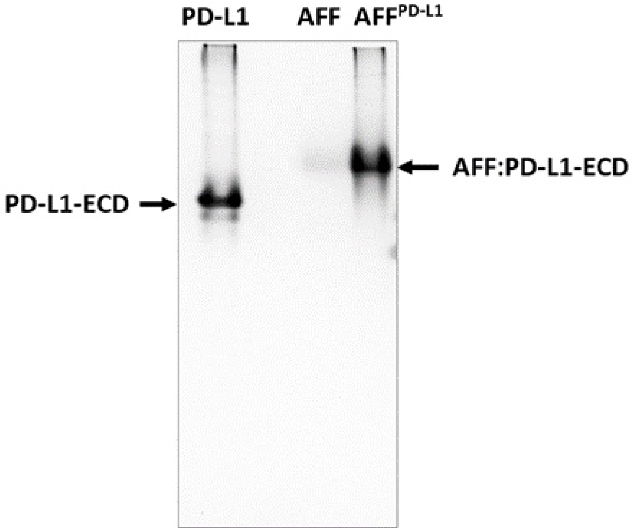

**Figure S2.** Successful preparation of anti-PD-L1 AFF. Binding between purified AFF-HIS and PD-L1-ECD-HIS was confirmed by Native-PAGE analysis.

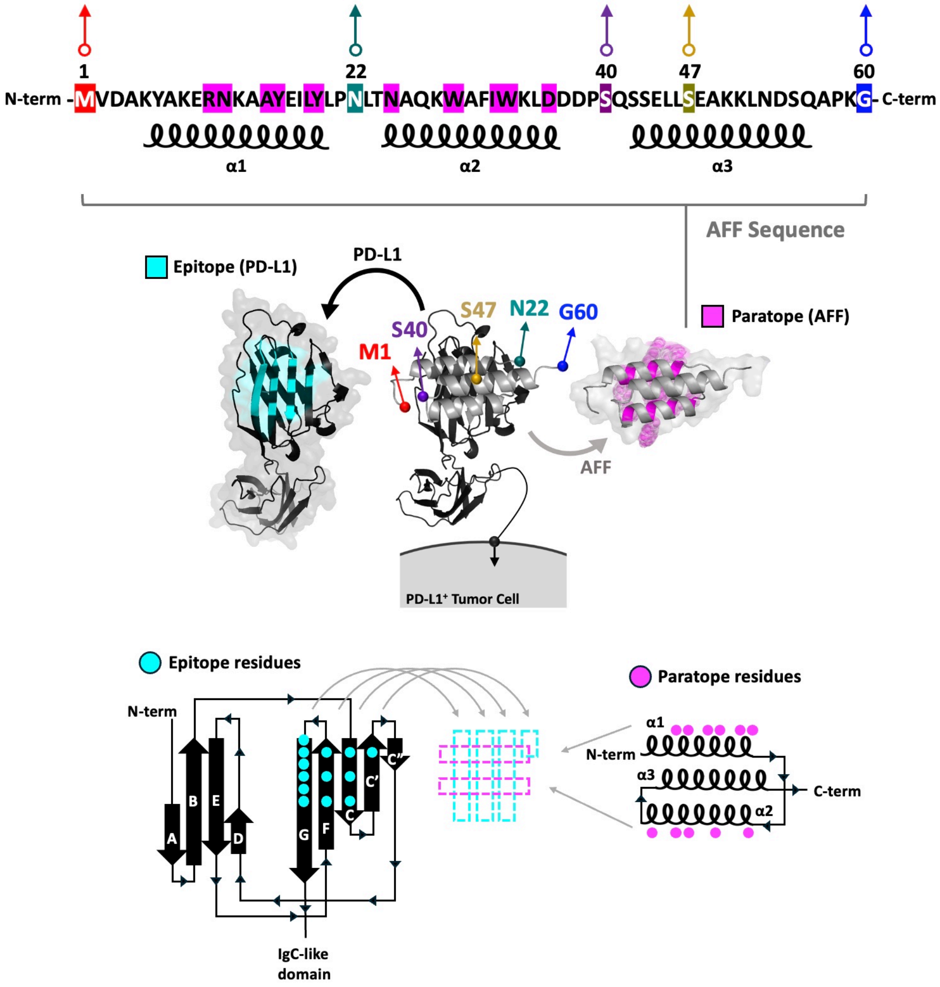

**Figure S3.** Five pulling geometries indicated based on the full AFF sequence with epitope and paratope information.

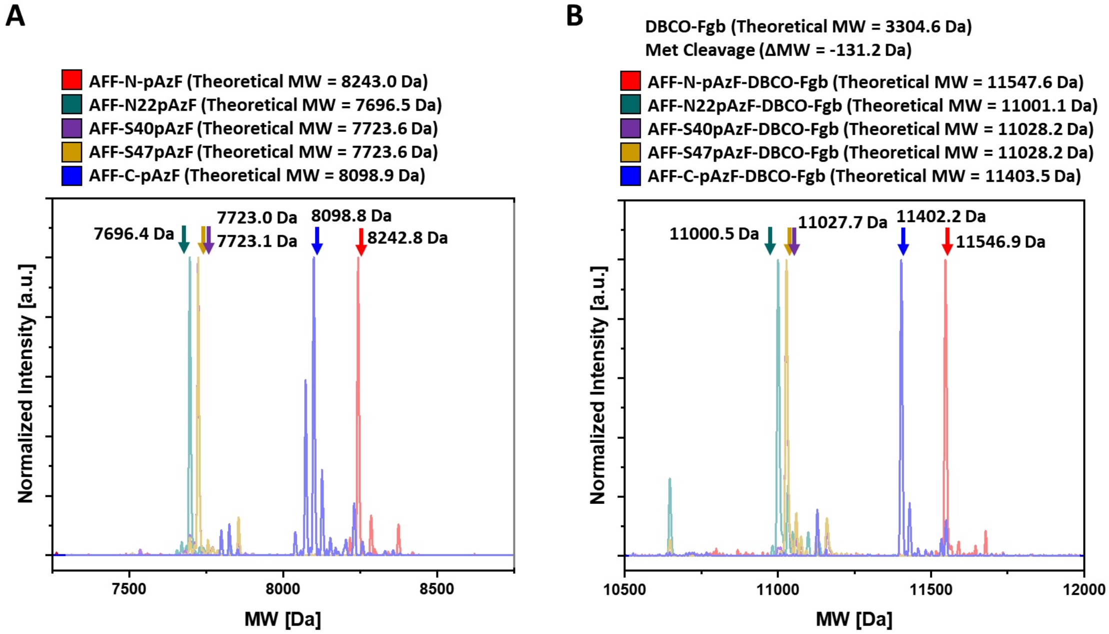

**Figure S4.** HRMS analysis of purified and conjugated AFF-pAzF variants. (A) MW of purified AFF-pAzF variants. (B) MW of purified Fgβ peptide-conjugated AFF-pAzF variants.

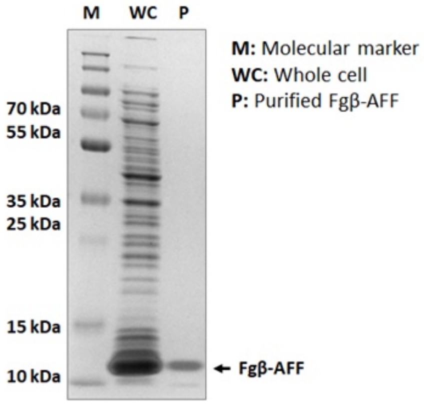

**Figure S5.** Successful preparation of Fgβ-AFF confirmed by SDS-PAGE analysis.

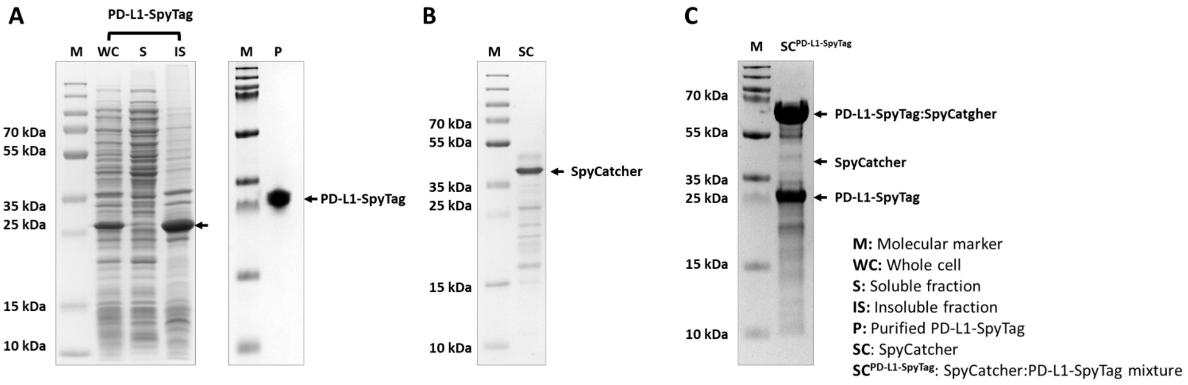

**Figure S6.** Recombinant PD-L1-SpyTag preparation and conjugation to SpyCatcher. (A) Successful expression and purification of PD-L1-SpyTag confirmed by SDS-PAGE analysis. (B) SpyCatcher preparation analyzed by SDS-PAGE. (C) Successful conjugation between PD-L1-SpyTag and SpyCatcher confirmed by SDS-PAGE analysis.

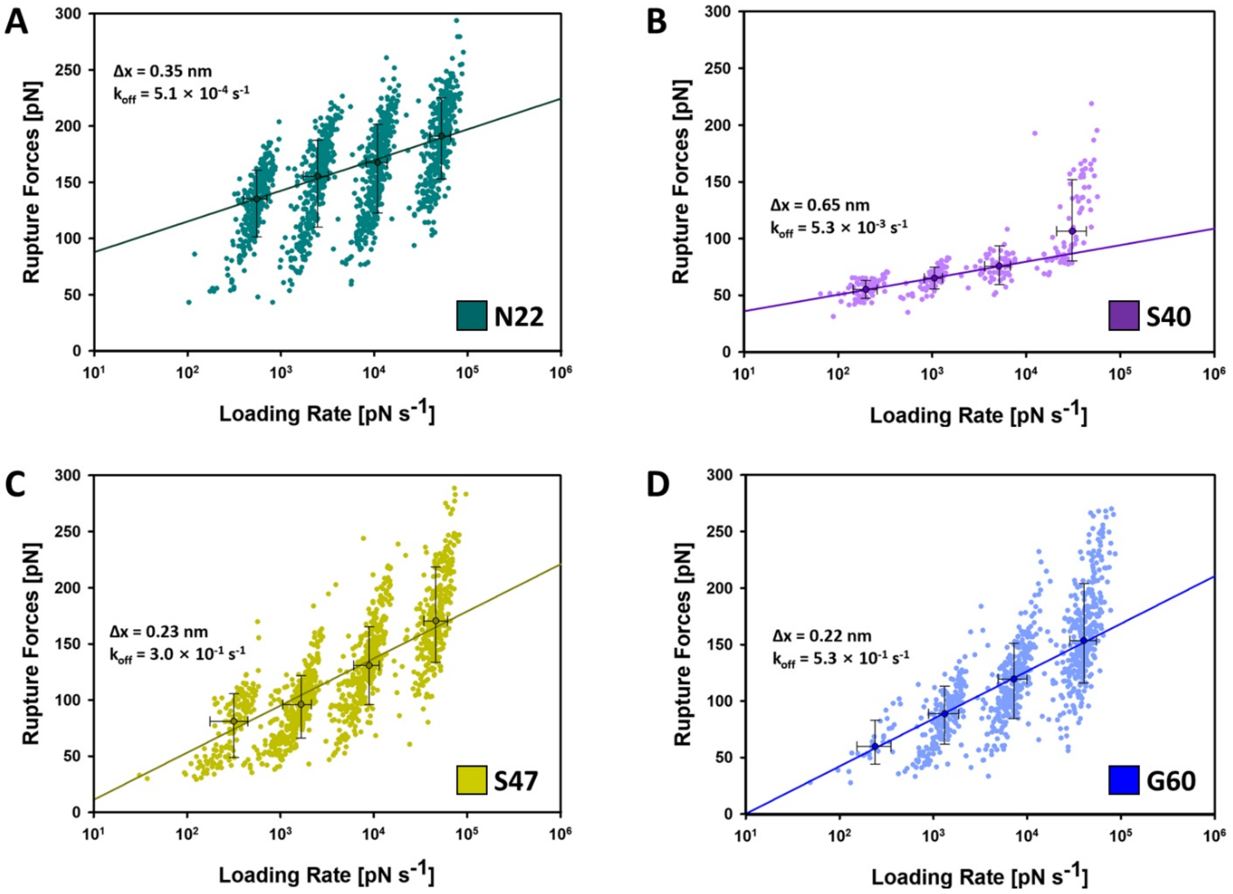

**Figure S7.** Dynamic force spectra of (PD-L1):AFF complex rupture events. (A) N22. (B) S40. (C) S47. (D) G60. Black-lined circles represent the median rupture force/loading rate at each pulling speed of $0.1 \times 10^3$, $0.4 \times 10^3$, $1.6 \times 10^3$, and $6.4 \times 10^3$ nm $s^{-1}$. Error bars are ±1 s.d. Solid and dashed lines are least square fits to the Bell-Evans (BE) model.

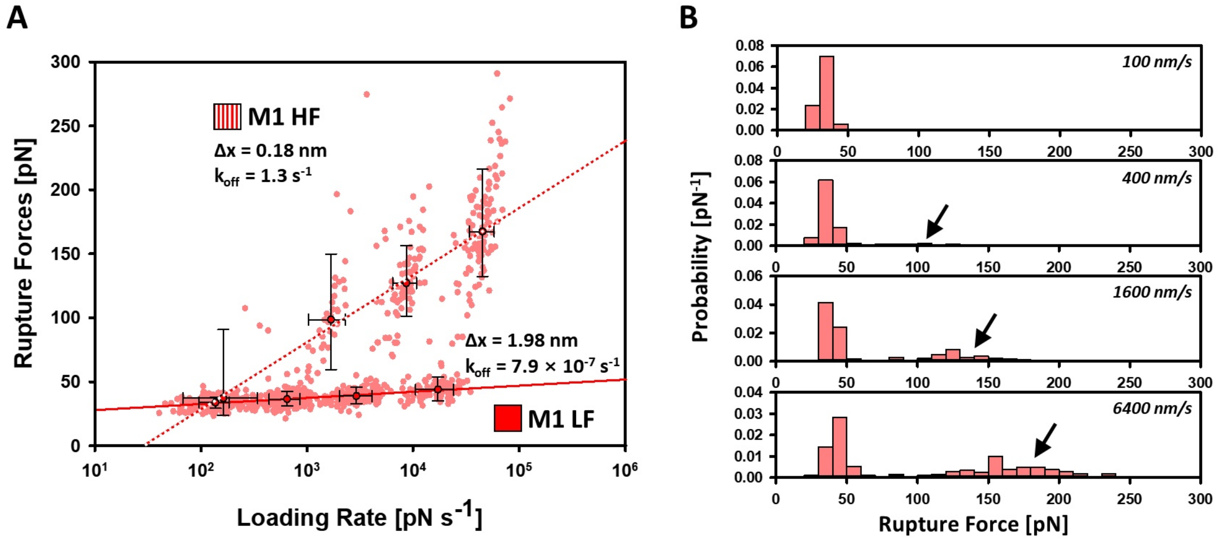

**Figure S8.** Catch bond-like behavior between the Fgβ-AFF:PD-L1 complex rupture. (A) Dynamic force spectra of the Fgβ-AFF:PD-L1 complex rupture. Black-lined circles represent the median rupture force/loading rate at each pulling speed of 0.1x10$^3$, 0.4x10$^3$, 1.6x10$^3$, 6.4x10$^3$ nm s$^{-1}$. Error bars are ±1 s.d. Solid lines are least square fits to the Bell-Evans (BE) model. (B) Histograms of the Fgβ-AFF:PD-L1 complex rupture probability at different pulling speeds and emergence of high force population (black arrows).

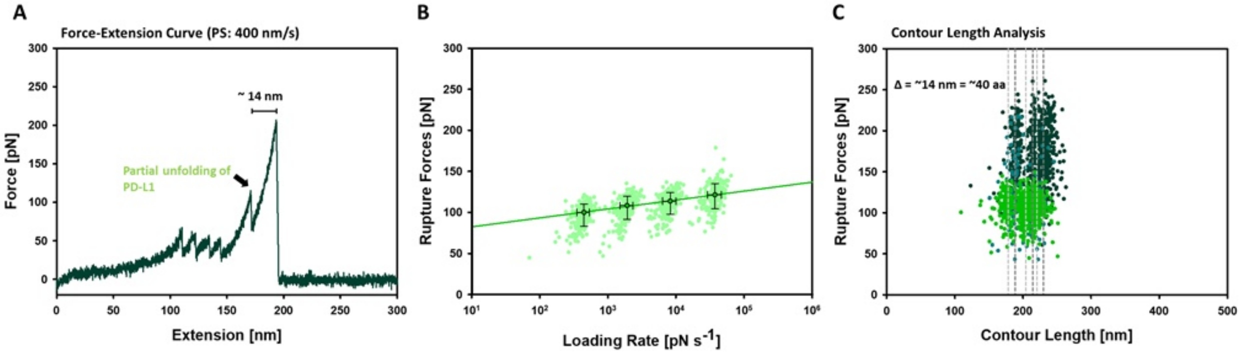

**Figure S9.** Partial unfolding of PD-L1 between the AFF(N22):PD-L1 complex rupture. (A) Typical AFM force−extension traces of the AFF(N22):PD-L1 complex rupture. Additional peak (Lime; partial unfolding of PD-L1) was observed prior to the final rupture between AFF and PD-L1. (B) Dynamic force spectra of the partial PD-L1 unfolding with a pulling geometry of N22. Black-lined circles represent the median unfolding force/loading rate at each pulling speed of $0.1 \times 10^3$, $0.4 \times 10^3$, $1.6 \times 10^3$, $6.4 \times 10^3$ nm $s^{-1}$. Error bars are ±1 s.d. Solid lines are least square fits to the Bell-Evans (BE) model. (C) Contour length analysis showing partial unfolding of PD-L1 as long as ~14 nm which is equivalent to ~40 amino acids long.

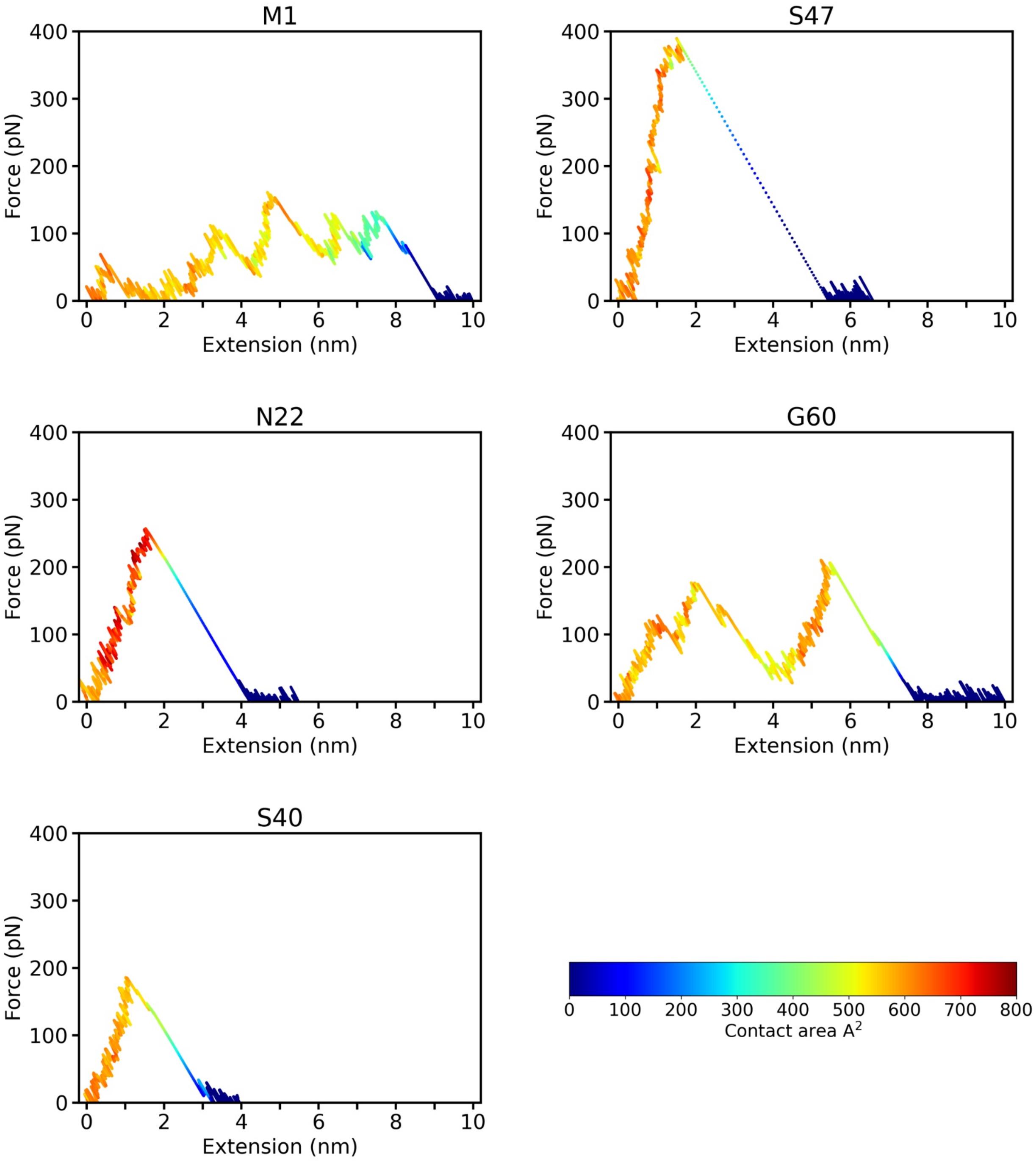

**Figure S10.** Typical force and contact area profiles steered molecular dynamics simulations, pulling at 2.5x10$^7$ nm s$^{-1}$. The dissociation frequently coincides with a sharp loss of contacts area when pulling from the internal residues (N22, S40, and S47), while pulling from the terminal residues (M1 and G60) reveal partial unfolding prior to the final rupture.

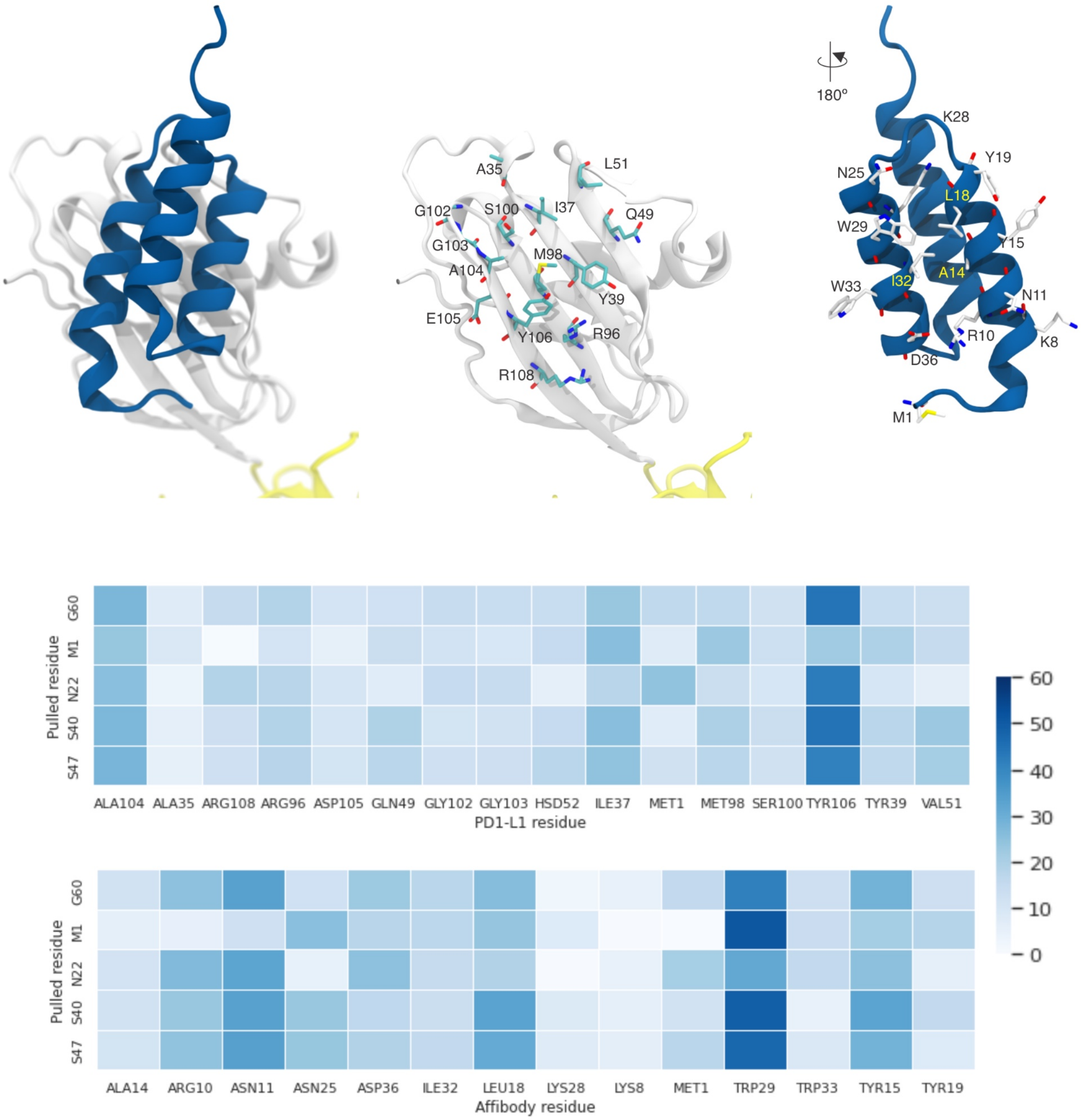

**Figure S11.** Mean PD1-L1:Affibody contact area in Å$^2$, as indicated in the color scale bar, over 40 replicas for the 5.0 ns before the Peak Rupture Force (2.5x10$^7$ nm s$^{-1}$)

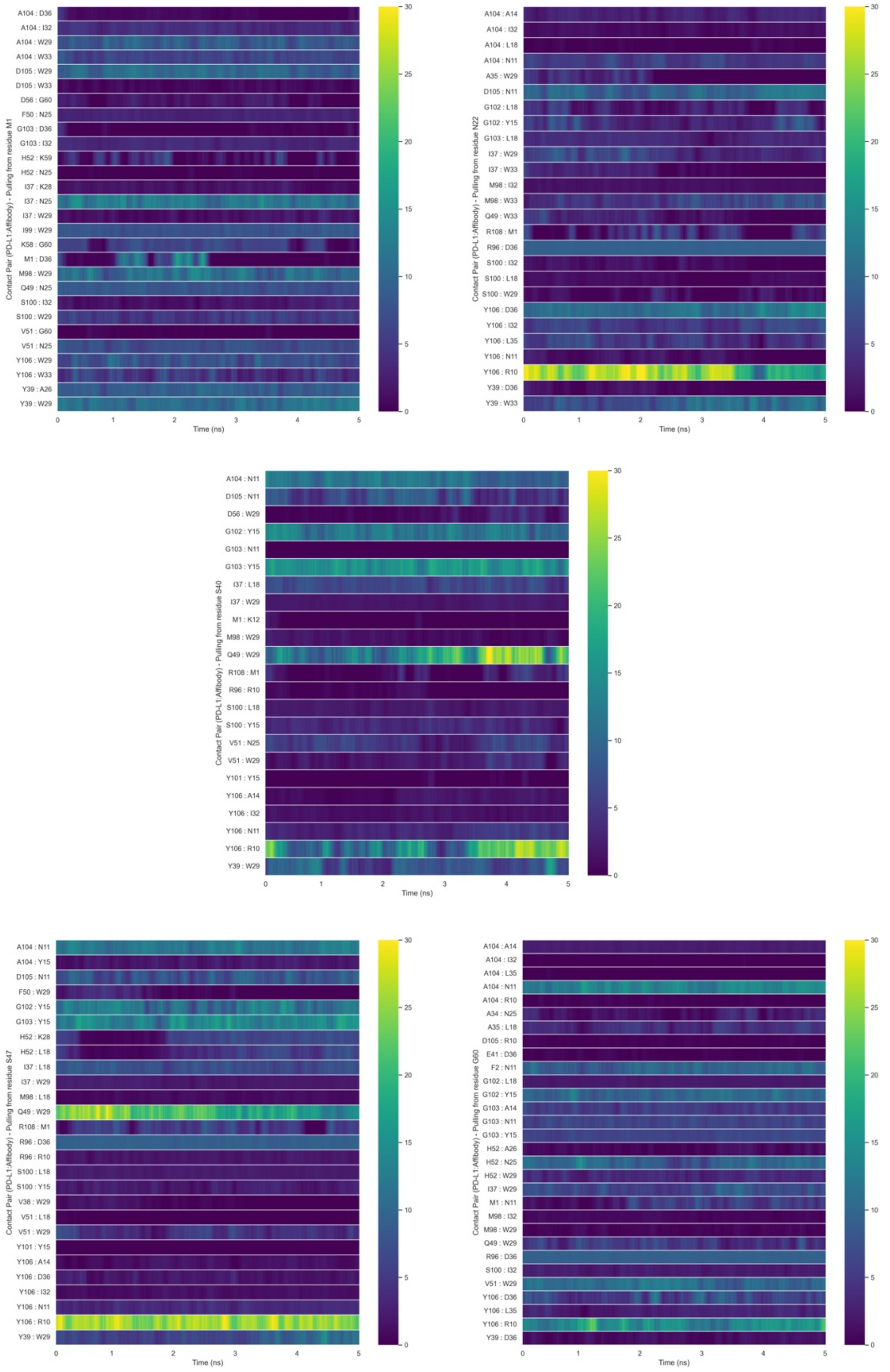

**Figure S12.** Exhibit of the contact area during the 5 ns prior to the maximum force for PD-L1:Affibody. Color scale bar in Å$^2$.

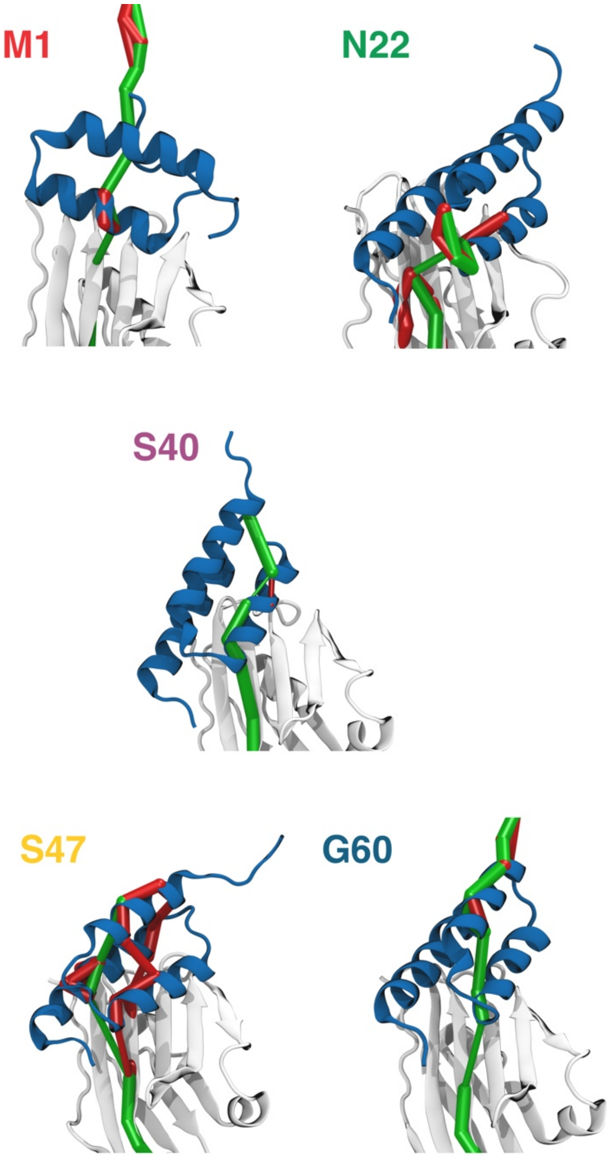

**Figure S13.** Zoom in on the binding interface showing the predominant force propagation pathways. The optimal force propagation path is colored in green, while the suboptimal propagation paths are colored in red.

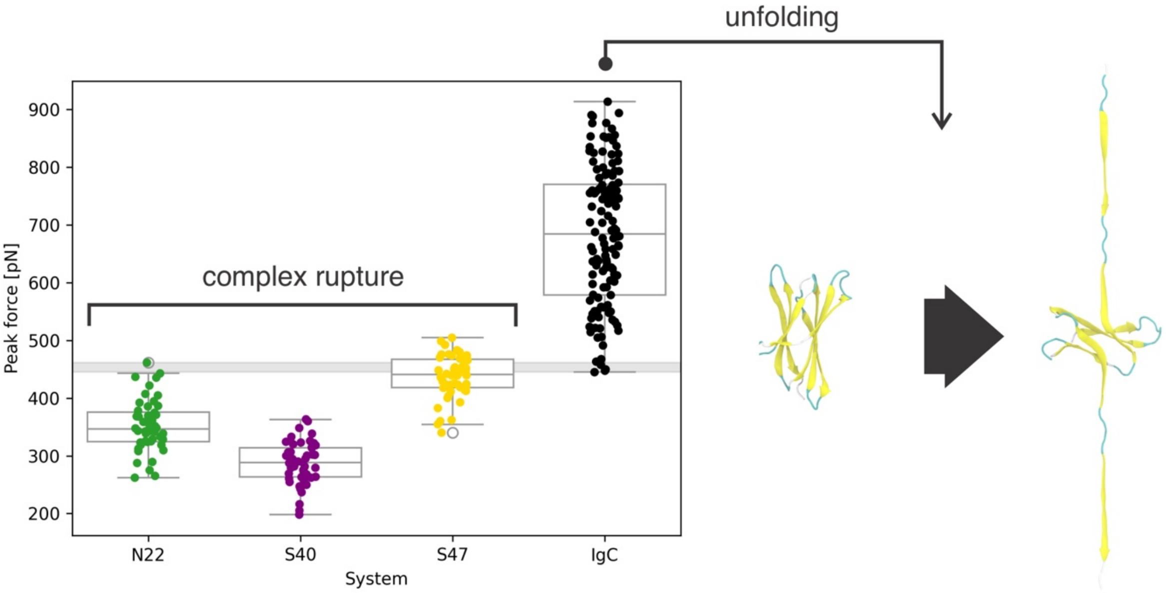

**Figure S14.** Pulling simulations at a rate of 2.5 x $10^8$ nm $s^{-1}$ demonstrate that the IgC domain can unfold at peak forces similar to those observed when pulling from the strongest anchoring points, N22 and S47.

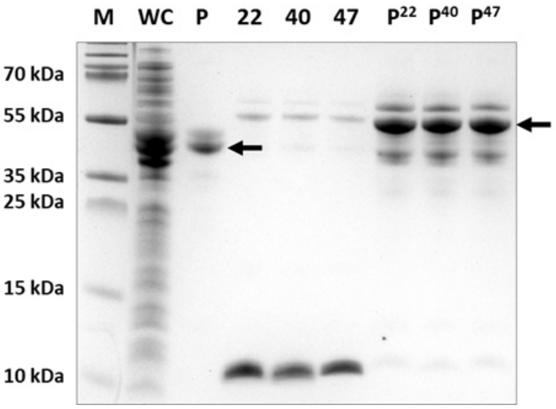

**M:** Molecular marker
**WC:** Wholecell of Cys-SpyCatcher
**P:** Purified Cys-SpyCatcher
**22:** **AFF-N22pAzF**
**40:** **AFF-S40pAzF**
**47:** **AFF-S47pAzF**
**$P^{22}$:** Purified after conjugation: **AFF-N22pAzF**
**$P^{40}$:** Purified after conjugation: **AFF-S40pAzF**
**$P^{47}$:** Purified after conjugation: **AFF-S47pAzF**

**Figure S15.** Conjugation between Cys-SpyCatcher and AFF-pAzF variants. Successful expression and purification of Cys-SpyCatcher and its following conjugation with AFF-pAzF variants were confirmed by SDS-PAGE analysis.

# SI videos

Puling from residue M1 (M1.mp4)
Puling from residue N22 (N22.mp4)
Puling from residue S40 (S40.mp4)
Puling from residue S47 (S47.mp4)
Puling from residue G60 (G60.mp4)

# References

63. Jobst, M. A., Schoeler, C., Malinowska, K. & Nash, M. A. Investigating receptor-ligand systems of the cellulosome with AFM-based single-molecule force spectroscopy. *J. Vis. Exp.* **82**, e50950 (2013)
64. Dudko, O. K., Hummer, G. & Szabo, A. Intrinsic rates and activation free energies from single-molecule pulling experiments. *Phys. Rev. Lett.* **96**, 108101 (2006).